Interface area density model for Large-Eddy Simulation of assisted atomization in fiber regime

F. Granger, J.-C. Hoarau, L.-H. Dorey, D. Zuzio, J.-L. Estivalezes

Interface area density model for Large-Eddy Simulation of assisted atomization in fiber regime

F. Granger[a,c], J.-C. Hoarau[a], L.-H. Dorey[a,*], D. Zuzio[b], J.-L. Estivalèzes[b]

[a] *DMPE, ONERA, Université Paris-Saclay, 91120 Palaiseau - France*
[b] *DMPE, ONERA, Université de Toulouse, 31000 Toulouse - France*
[c] *CNES - Transport Spatial - Etablissement Daumesnil, F-75612 Paris Cedex, France*

Abstract

In the context of simulating liquid rocket engines (LREs), accurately reproducing the complex combustion chamber environment poses a significant challenge. Recent works have shown that Direct Numerical Simulation has made good progress in achieving the simulation of the whole range of temporal and spatial two-phase flow scales involved. However, due to the computational costs, it is currently out of reach in an industrial context. Large-Eddy Simulations (LES) considerably reduce the computational cost but require modeling the two-phase flow at sub-grid level. A promising approach for such modeling is the interface area density (IAD) approach, which was developed initially for LES of flame fronts and subsequently adapted to Diesel jet atomization to recover spray droplet size distributions. In this method, a subgrid density of interface area is transported with an advection equation, while opportune source terms simulate its growth by breakup or its reduction by coalescence effects. In the context of the LREs assisted atomization, the complex mechanism of the assisted atomization in fiber regime must be taken into account by the subgrid model to recover the correct spray size distribution. The present work proposes a new interface area density evolution modeling for two-phase LES of coaxial assisted atomization in fiber regime. The proposed model focuses on recovering a realistic liquid-gas relative velocity at all the scales, enabling accurate modeling of sub-grid scales by using the IAD as a measure of liquid structure sizes.

Keywords: Liquid rocket engine, Fiber regime, Two-phase flow, Assisted atomization, Interface area density

1. Introduction

Atomization is the process by which a coherent liquid jet disintegrates into numerous independent structures. It finds many industrial applications such as agriculture, paint, and fuel injection. In most cases, the liquid is injected into a quiet atmosphere, resulting in a mechanical atomization piloted by turbulence. Conversely, in the constrained environment of combustion chambers, injectors of various shapes, either rectangular [1, 2, 3, 4], annular, or round [5] employ the so-called assisted atomization to pulverize the large mass-flow rates needed by the combustion chamber: a high-velocity gas stream accelerates the liquid, triggering two-phase instabilities which lead to the liquid atomization. During the development of a liquid rocket engine (LRE), several injector types and configurations are tested to ensure maximum performance and to check for possible combustion instabilities, which may lead to engine self-destruction, especially during the ignition phase. Numerical simulation offers a way to explore combustion instabilities, but it requires an accurate estimation of the couplings between the flame, the mechanical structure, and the liquid jet. Particularly, the precise measurement of the local liquid structure's size is crucial since the interaction between droplets and acoustics in the chamber is significant.

A significant challenge arises with coaxial injectors typically used in LRE, which generate complex liquid structures that can break up in droplets of a few microns [6] over a distance of several centimeters from the injection plane, depending on the regime. Some experimental studies have tackled the hard task of describing the atomization process and measuring granulometry using, among other techniques, laser-based techniques [7] or shadowgraphy imaging [5, 8]. These techniques have made it possible to observe different breakup regimes, but, despite the progresses that have been made, they can still only achieve a limited resolution or study a small part of the spray due to the very dense and multi-scale two-phase flow.

On the other hand, Direct Numerical Simulation (DNS) offers a way to simulate the atomization process and provide a large amount of detailed data on the liquid topology. Simulations of a coaxial liquid jet were first performed with Volume-Of-Fluid (VOF) approach [9, 10] at low Reynolds and Weber numbers, concentrating on the behavior of the intact liquid core and its instabilities. A coupled VOF/Level-Set/Large Eddy Simulation approach was proposed in [11] for a wider range of Weber numbers, up to the formation of a spray. More recent work based on the opensource software OpenFOAM [12] investigated the effect of several parameters on the primary atomization of a coaxial liquid jet at high Weber and Reynolds numbers [13, 14], such as the nozzle up-scaling and pressure. However, these works are still confronted to the inability to predict the flow small-scale characteristics, and in particular the size of the

*Corresponding author
Email address: luc-henry.dorey@onera.fr (L.-H. Dorey)

Nomenclature

Greek symbols

α	volume fraction
Δ	cell size (m)
δ'_ω	slope of vorticity thickness
η	similarity parameter
λ_{atom}	atomization indicator function
μ	dynamic viscosity ($kg.m^{-1}.s^{-1}$)
Ψ	resolution indicator function
ρ	density ($kg.m^{-3}$)
Σ	interface area density (m^{-1})
σ	surface tension ($kg.s^{-2}$)
τ	characteristic time scale (s)

Latin symbols

δS	area (m^2)
δV	volume (m^3)
A	large scale production time (s)
a	small scale production time (s)
a_λ	driving atomization indicator function coefficient
b_λ	position atomization indicator function coefficient
D	injector diameter (m)
d	drop diameter (m)
D_s	turbulence diffusion coefficient ($m^2.s^{-1}$)
f	frequency (s^{-1})
h	gas injector thickness (m)
K	velocity decay coefficient
k	turbulent kinetic energy ($m.s^{-1}$)
L	characteristic length scale (m)
R	non dimensional injector transverse coordinate
r	distance from the axis (m)
$Re_{a,b}$	Reynolds number based on phase a and length b
$S_{i,j}$	strain tensor (s^{-1})
T_m	mixing layer thickness (m)
U	injection velocity ($m.s^{-1}$)
u	local velocity ($m.s^{-1}$)
We_p	Weber number of phase p
X	non dimensional injector axis coordinate
x	injector axis coordinate (m)
IAD	interface area density
LRE	liquid rocket engine
MFR	mass flow ratio
Oh	Ohnesorge number
VOF	volume of fluid

Superscripts

$'$	sub-grid
$*$	non dimensional

Subscripts

∞	far field
g	gas
l	liquid
p	production
t	turbulence
atom	atomization phenomenon
axis	injector axis
co	collision
cr	critical value
DNS	direct numerical simulation
LES	large eddy simulation
max	maximum velocity in plane
rec	reconstructed term
res	resolved part

spray after primary (and secondary) atomization. The work of [15] focused again on the liquid core, examining the effect of the injection condition and the flow near injector lip up to a contact-angle problem. Despite these efforts, it remains a challenge to simulate the full range of two-phase flow scales of the entire spray, as it naturally requires extremely large meshes to resolve the smallest scales. Recent work attempted to simulate of the full scale of atomization using a massive coupled VOF/Level-Set simulation on a near 3 billions mesh cells [16], which for the first time explored and correlated the full distribution of liquid volume and surface in space, together with the detection and classification of isolated liquid structures.

However, the sheer CPU cost of this simulation makes it impractical in an industrial setting. To reduce computational costs, Reynolds-Averaged Navier-Stokes (RANS) or Large Eddy Simulation (LES) approaches attempt to overcome this problem by using semi-empirical models to inject an Eulerian or Lagrangian sub-grid dispersed phase into the numerical domain [17, 18]. Despite their advantages, these models often ignore the complex phenomena in the dense zone close to the injector.

Several authors have identified the relevant non-dimensional parameters that classify atomization regimes and provide correlations to estimate atomized liquid structure sizes. Reynolds and relative Weber numbers were determined to correlate injection conditions to the flow regime for round jets [19], coaxial jets [20, 5], and cross-flowing liquid jets [21, 22]:

$$\mathrm{Re}_{l,L} = \frac{\rho_l U_l L}{\mu_l} , \tag{1}$$

$$\mathrm{We}_L = \frac{\rho_g (u_g - u_l)^2 L}{\sigma} . \tag{2}$$

with ρ the density, U the velocity, L a characteristic length, μ the dynamic viscosity of the liquid l or the gas g and σ the surface tension of the liquid in the gas phase. In addition, a gaseous Weber number defined by:

$$\mathrm{We}_g = \frac{\rho_g u_g^2 L}{\sigma} , \tag{3}$$

is used by Lasheras and Hopfinger [23] to define the different atomization regimes. In particular, the fiber regime encountered in LRE combustion chambers is characterized by high gas Weber and liquid Reynolds numbers, $\mathrm{We}_g \gtrsim 100$, $\mathrm{Re}_{l,L} \gtrsim 2000$, and high momentum ratio $J > 1$ [23, 24]. Under these conditions, the shearing effect of the gas induces a succession of KelvinHelmholtz and RayleighTaylor instabilities at the gasliquid interface, triggering the formation of thin ligaments that are stripped from the liquid jet and produce small droplets. Marmottant and Villermaux [5] derived an average drop size empirical law depending on the injection liquid Reynolds ($\mathrm{Re}_{l,L}$) and Weber (We_L) numbers, although it provides only a time and space averaged value. Thus, available correlations can not provide a local drop size dependent on the local flow conditions, which is required for a precise coupling of the liquid jet with the acoustics.

The limitations of the existing correlations have motivated the development of new approaches to evaluate the local and instantaneous drop size in the atomization process. One promising way is to use a statistical approach, in which a characteristic sub-grid length scale is recovered in each interface cell from the resolved fluid quantities. The Eulerian-Lagrangian Subgrid Atomization (ELSA) model from [25, 26] was explicitly designed to describe the atomization of flows with high Weber and Reynolds numbers. This approach is valid under two conditions: the Reynolds and the Weber number of the flow must be sufficiently large, so turbulence is predominant, and the interfacial forces can be neglected in front of the kinetic energy of the liquid-gas mixture. These assumptions allow to use a single momentum and mass conservation equation, a "one fluid" approach. The principle of the ELSA model is that the sub-grid interface topology can be statistically represented by the quantity of liquid/gas interface, known as the interface area density (IAD). The salient feature of the model comes from the fact that it does not assume that the liquid phase consists of spherical drops, settling it apart from the dispersed phase approaches. Besides, the model is meant to work mainly in the dense primary atomization regions, where the liquid topology is seldom in the form of spherical droplets. Initially developed by Marble and Broadwell [27] to model the flame front sub-grid wrinkling, the quantity of interface within the cell or local interface area density can be defined as a function driven by an exact equation [28], which has to be closed. The interface area density Σ can be written as the ratio between the interface area δS and a given control volume δV:

$$\Sigma(\mathbf{x}, t) = \delta S / \delta V . \tag{4}$$

The general form of the Σ evolution can be modeled by a transport-diffusion equation with multiple source terms. These source terms account for various physical phenomena such as turbulent mixing between the liquid and gas phases, mean shear stress, breakup, and destruction caused by coalescence or vaporization. The formulation given by Vallet et al. [25] for RANS applications is the following:

$$\frac{\partial \overline{\Sigma}}{\partial t} + \frac{\partial (\widetilde{u}_i \overline{\Sigma})}{\partial x_i} = \frac{\partial}{\partial x_i}\left(D_s \frac{\partial \overline{\Sigma}}{\partial x_i} \right) + (A + a)\overline{\Sigma} - V_s \overline{\Sigma^2} , \tag{5}$$

with $\overline{\Sigma}$ being the average interface area density, D_s a diffusion coefficient, A and a respectively large and small scale characteristic production times, and V_s a coalescence coefficient. Vallet et al. [25] modeling approach assumes the existence of a critical local Weber number ($\mathrm{We}_{\mathrm{cr}}$) at which the shearing and capillary forces balance each other, leading to the cessation of the atomization cascade. The closure terms for the IAD transport equation were mostly derived from single-phase turbulence concepts. An interesting assumption made in the Vallet et al. [25] model is that there must exist an equilibrium liquid droplet diameter characterizing this balance for $\mathrm{We}_{\mathrm{cr}} = 1$.

In recent years, there has been increasing interest in developing accurate numerical simulations of multiphase flows, particularly those involving complex interface area density equations. Based on the work of [25], Jay et al. [29] presented a cryogenic injector reacting flow simulation using an Arbitrary Eulerian-Lagrangian (ALE) multi-fluid approach coupled with both interface and flame density equations. The resulting IAD equation source term is rather complex, with two production terms: one by shearing effects near the injector instabilities and the other by the Taylor Analogy Breakup (TAB) [30]. The simulation results agreed well with experimental measurements of average interface area density and heat flux. Similarly, Lebas et al. [31] used the ELSA model to simulate the dense region of a Diesel jet, employing a split between a "dense" and a "dilute" zone based on the local value of the phase function (liquid mass fraction). In this case, two IAD source terms were active in the dense (turbulent source $[\cdot]_t$) and dilute (collision source $[\cdot]_{co}$) regions respectively, driven by a characteristic time $\tau_{t,\mathrm{co}}$ that rules the growth of Σ as given in equation (6):

$$\dot{\overline{\Sigma}}_p = \frac{\overline{\Sigma}}{\tau_{t,\mathrm{co}}} \left(1 - \frac{\overline{\Sigma}}{\overline{\Sigma}_{t,\mathrm{co,cr}}} \right) , \tag{6}$$

with $\overline{\Sigma}_{t,\mathrm{co,cr}}$, the critical $[\cdot]_{\mathrm{cr}}$ IAD characterizing the equilibrium IAD value. This approach was employed with a single-phase

flow model, in which the fluid is composed of two species, liquid and gas, with highly variable density. As in [25], geometrical and turbulent quantities were used to model these values. Comparisons were made with the Beau et al. [32] model and a DNS from the CORIA ARCHER code. Duret et al. [33] performed Level-Set/VOF DNSs to measure the critical Weber number. The liquid was immersed in an Isotropic Homogeneous Turbulent (IHT) field in a three-dimensional cubical domain with periodic boundaries. A statistical analysis of the equilibrium Weber number was performed to verify the definition given by the ELSA model for various liquid volume fractions, mesh resolutions, and surface tensions. This study suggested using liquid kinetic energy or Favre averaged kinetic energy in the equilibrium Weber number.

Chesnel et al. [34] attempted an extension of [25] and [31] interface area density approach to the LES simulation of a Diesel jet. They introduced a decomposition of the interface area density into resolved and sub-grid parts consistent with the LES approach. The minimum resolved interface area density Σ_{min} is reconstructed for theoretical spherical cells and is given by the following equation:

$$\Sigma_{\text{min}} = 2.4\sqrt{\alpha_l(1-\alpha_l)}\,, \tag{7}$$

with α_l the liquid volume fraction. The splitting ensures the convergence of the resolution of increasingly smaller scales towards a DNS. Moreover, when the interface is sufficiently resolved, the total interface area density should tend towards the value resolved by the LES mesh. They also proposed a formulation for the critical Weber number, which is given as:

$$\text{We}_{\text{cr}} = \alpha_l(1-\alpha_l)\frac{\overline{\rho}\widetilde{k_g}}{\sigma\Sigma'_{\text{cr}}}\,, \tag{8}$$

with $\widetilde{k_g}$ the filtered sub-grid kinetic energy and Σ'_{cr}, the sub-grid critical IAD. In consequence, the critical threshold of interface area density takes the following form:

$$\Sigma_{cr} = \Sigma_{\text{min}} + \alpha_l(1-\alpha_l)\frac{\overline{\rho}\widetilde{k_g}}{\sigma\,\text{We}_{\text{cr}}}\,. \tag{9}$$

The practical value of the critical Weber number is set to 1 as for Vallet et al. [25], indicating a state of equilibrium between turbulent energy and surface tension forces. Additionally, the assumption of turbulent atomization is adopted for the characteristic time, which is determined using a Boussinesq-like approximation as follows:

$$\frac{1}{\tau_t} = |\overline{S}| = \sqrt{2\overline{S}_{i,j}\overline{S}_{i,j}}\,, \tag{10}$$

with

$$\overline{S}_{i,j} = \frac{1}{2}\left(\frac{\partial\overline{u}_i}{\partial x_j} + \frac{\partial\overline{u}_j}{\partial x_i}\right). \tag{11}$$

The so-formulated sub-grid IAD model for the LES formalism has given promising results on Diesel jets with mechanical atomization.

In the particular configuration of the coaxial assisted atomization in fiber regime, the several hypotheses made in the previous work are not adapted to the nature of the flow. In particular, in high-energy assisted atomization, the liquid destabilization and breakup are expected to originate from the interfacial instabilities rather than from turbulent effects alone. The critical Weber number should also be a function of the local shear effect, as the liquid structures tend to the local equilibrium with the gas as they travel downstream. This study's proposed model aims to take into account this particular physical phenomenon. In the same way as for the original ELSA formulation, the model is built to work together with a dense two-phase solver, able to simulate the largest scales of primary atomization, its goal being to recover a local characteristic liquid surface. This value may be used for several purposes, among them as an initial diameter for a dispersed phase model (similar to a D32 diameter) or as an input for a phase-change model, wherever the multi-fluid solution becomes poorly resolved on the LES mesh. In the presented paper, the model is coupled to a diffuse interface multi-fluid model.

The model is based on the same transport-diffusion equation as Chesnel et al. [34] with a redefined source term. The proposed formulation for the critical Weber number defined in Equation 2 relies heavily on the relative velocity between the gas and the liquid. To this purpose, an innovative method to estimate the liquid/gas relative velocity is presented. The adapted model is then applied in an LES simulation of a coaxial injector under LRE conditions, and the results are compared to DNS reference data for validation.

2. Configuration

The study investigates a single coaxial injector typical of an LRE, designed to produce a fiber regime atomization in the chamber. The configuration is based on an experimental setup from Ficuciello et al. [35] to study the effect of acoustics on a water/air spray. This configuration was investigated numerically by Rutard et al. [36] with the ONERA multiphase flow code CEDRE. This geometry was also studied by Hoarau et al. [16] at a lower density ratio to improve the DNS robustness. This work provided a detailed analysis of the flow focusing on the atomization process with precise IAD measurements, unavailable from experimental sources, that were used to develop and validate the model proposed in the present paper. That is why conditions in this paper were chosen identical to the DNS of Hoarau et al. [16] while Reynolds numbers, Weber number and momentum ratio remain identical to the previous studies [36, 16] and correspond to fiber-type atomization regime as defined by Lasheras and Hopfinger [23]. The actual parameters used in the present paper are given in Table 1 along with the ones of the two previous studies.

Depiction of a typical two-phase field encountered from a coaxial injector in fiber regime is drawn in Figure 1, with D_l the liquid injection diameter, and h_g the thickness of the gas ring.

	LES [36]	DNS [16]	present LES
Domain dimensions $[L_x/D_l, L_y/D_l, L_z/D_l]$	$10.7 \times 8.9 \times 8.9$	$18.6 \times 5.8 \times 5.8$	$11 \times 5.8 \times 5.8$
Liquid/gas density ratio	~ 1000	~ 100	~ 100
Momentum ratio	4	4	4
Re_l	5×10^3	5×10^3	5×10^3
Re_g	$\sim 10^4$	$\sim 10^4$	$\sim 10^4$
We_g	4.9×10^2	4.9×10^2	4.9×10^2

Table 1: Simulation data from [36], DNS [16] and the LES of the study

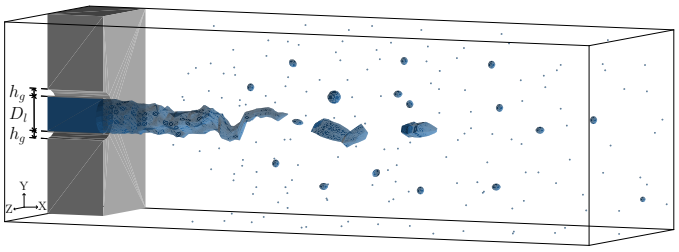

Figure 1: Scheme of coaxial injection in fiber regime

2.1. Computational framework

In this study, the proposed model works within a computational LES framework for solving dense multiphase flows. The framework consists of the CEDRE software platform, which has already been successfully employed to simulate similar flows in Le Touze et al. [37] and [36]. CEDRE is based on the compressible multiphase, multi-specie Navier-Stokes equations discretized by a Finite Volume approach on general unstructured meshes. The multiphase model can handle an arbitrary number of phases. Within this work, a two-phase, gas and liquid, flow is considered: the model becomes a diffuse interface approach based on the homogeneous relaxation, also referred to as the 4-equation model. It is a simplified model obtained by imposing infinitely fast relaxations on the original Baer-Nunziato 7-equations model [38]. Consequently, in each control volume, there exists only one velocity, one pressure and one temperature, besides the mass concentrations of species and phases. Therefore, the equilibrium hypothesis does not allow the modeling of momentum or temperature in-cell exchanges. As the diffuse interface method is not suited to resolve the small liquid structures composing the spray, it is used in this work to solve the largest primary atomization scales and feed the proposed ISD model. The modeling of the spray generated by the liquid atomization is usually done in CEDRE by dynamically switching to appropriate statistical dispersed phase models (they will not be used in this paper). One possible application of the ISD model would be to give information on the characteristic size of the dispersed phase during the dense-dispersed transition.

The 4-equation model is expressed as the equation system (12) for the conserved quantities $\mathbf{Q}(\mathbf{U}) = \left(\rho Y_l, \rho Y_g, \rho u, \rho e_t\right)^t$, with Y the mass fraction for either the liquid or the gas, u, ρ and e_t the mixture velocity, density and total energy. The conserved quantities are function of the natural variables $\mathbf{U} = (Y_l, Y_g, p, T, \mathbf{u})^t$.

$$\frac{\partial \mathbf{Q}}{\partial t} + \nabla \cdot (\mathbf{F} - \psi_D - \psi_C) = 0 \,, \tag{12}$$

where $\nabla \cdot ()$ is the divergence operator. Since no mass transfer was considered and gravity was considered as in-influential for the considered flow, no source term appears on the right-hand side of (12). The density ρ of the mixture is computed as $\rho = \rho Y_l + \rho Y_g = \alpha_g \rho_g + \alpha_l \rho_l$, with $\alpha_i = \rho Y_i / \rho_i$ the i-th phase volume fraction. The phase volume fractions are obtained by imposing volume conservation through the equations of state of each phase, function of local pressure, temperature and bulk phase densities ρ_g and ρ_l (see [37] for details). The considered equations of state are perfect gas, $p = \rho RT$ and weakly compressible liquid, $p_l(p) = \rho_0[1 + \beta_0(p - p_0)]$, β_0 being the isothermal compressibility at the reference state p_0, ρ_0.

In system (12), the convective flux are written as $F = [Q \otimes \mathbf{u} + p(0, 0, \mathbf{I}, \mathbf{u})^t]$, with I the identity tensor and $\otimes$ the tensor product. The diffusive fluxes read $\psi_D = [0, 0, \tau, (\tau \cdot \mathbf{u} + \lambda \nabla T)]^t$, where λ is the thermal conductivity. Heat diffusion is considered even if the proposed test case is isothermal. Inter-specie diffusion may be considered in the bulk phases, though single-specie phases were used in this work. For the turbulence modeling, Boussinesqs eddy viscosity model is adopted, so that the viscous stress tensor can be written in function of the resolved symmetric strain rate tensor as:

$$\tau = 2(\mu + \mu_t)\mathbf{D}, \text{ with } \mathbf{D} = \frac{1}{2}[\nabla \otimes \mathbf{u} + (\nabla \otimes \mathbf{u})^t] - \frac{1}{3}(\nabla \cdot \mathbf{u})I \,. \tag{13}$$

The modeling of the turbulent viscosity is done via the formulation proposed by Nicoud et al. [39]. It is based on the three singular values of the local velocity gradient tensor $\sigma_1 \geq \sigma_2 \geq \sigma_3 \geq 0$, which are used to express the subgrid turbulent viscosity as:

$$\mu_t = \rho (C_\sigma \Delta)^2 \frac{\sigma_3(\sigma_1 - \sigma_2)(\sigma_2 - \sigma_3)}{\sigma_1^2} \,, \tag{14}$$

with the constant $C_\sigma = 1.35$ and Δ the local size of the mesh. This model was designed to have better intrinsic properties than

existing formulations. In particular, it has the appropriate behavior close to solid boundaries, which is an important property for downstream mixing layer simulation. Finally, the turbulent frequency is given by $f_t = (2\mathbf{D} : \mathbf{D})^{1/2}$.

Surface tension is implemented via the Continuum Surface Force of Brackbill [40] written in the conservative formulation, Continuum Surface Stress, as proposed by [41]. The capillary fluxes read $\psi_C = [0, 0, \tau_C, (\tau_C \cdot \mathbf{u})]^t$, with the capillary stress tensor written as:

$$\tau_C = \sigma \|\nabla \alpha_l\| \left(\frac{\nabla \alpha_l}{\|\nabla \alpha_l\|} \otimes \frac{\nabla \alpha_l}{\|\nabla \alpha_l\|} - I \right), \tag{15}$$

with σ the coefficient of surface tension. (15) can be extended to a number of phases greater than two.

To limit the numerical diffusion of the interface, an interface sharpening method, originally developed by Chiapolino et al. [42], has been implemented and used in this study [43].

2.2. Meshes and convergence study

The proposed model is designed to work together and complement the dense two-phase solver introduced in the previous section, simulating the largest scales of the primary atomization. The accuracy of the dense phase solution can significantly impact the model's behavior, as the former implicitly defines a two-phase cut-off scale separating the "resolved" scales from the "subgrid" scales. For this reason, the following study will assess the behavior of the model on three increasingly fine LES mesh sizes (LES-M5, LES-M9 and LES-M20): the sought outcome is to recover relative mesh independence, where the model can recover the unresolved scales on any of the meshes. The cell number of each mesh is reported in Table 2.

	LES-M5	LES-M9	LES-M20
Cell number	$5.2M$	$9M$	$20M$

Table 2: LES mesh configurations

To compare the cell size between the different cases, the transverse-averaged cell size in the atomization zone for the three LES and the DNS from Hoarau et al. [16] are shown in Figure 2. The cell size is computed using the hydraulic diameter Δ, which provides consistent results regardless of the cell type used:

$$\Delta = \frac{6 V_{\text{cell}}}{S_{\text{cell}}}. \tag{16}$$

Figure 2 gives the scope of cell size in the atomization zone identified on the DNS. The LES-M20 mesh shows cell diameters of the same order of magnitude as the DNS ($\sim 0.22\,\Delta/\delta_{\text{lip}}$) in the atomization zone.

The LES-M9 mesh will be used to validate the IAD model, whereas the other meshes will be employed to test mesh convergence. The atomization process occurring is presented for the LES-M9 case in an instantaneous field on Figure 3. The

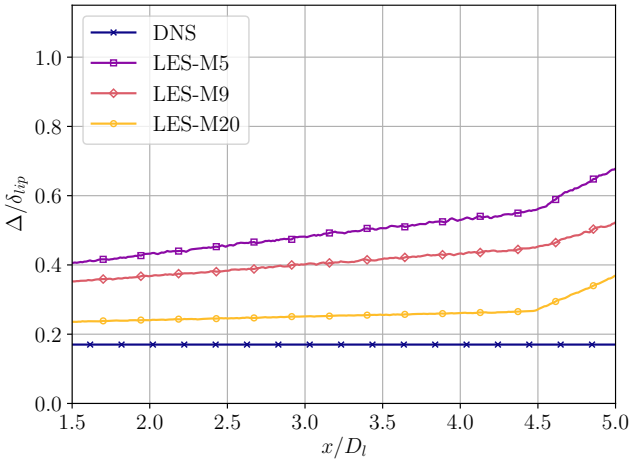

Figure 2: Average cell size in the atomization zone

plot shows an instantaneous field of the liquid volume fraction α_l, in yellow the liquid-filled cells, in blue the gas-filled cells, cut on the centerline of the injector. The picture shows the clearly visible liquid conical dart, spanning some diameters in the streamwise direction. The dart undergoes a longitudinal large-scale oscillation under the effect of the shearing gaseous flow. At the same time, thin ligaments ("fibers") are created by shear stress-induced instabilities on its surface, which give the name to the particular primary atomization process. Large liquid structures detach from the main body, near the axis of the jet, due to the thinning of the liquid and its oscillations. These ligaments undergo further breakup up to the formation of a population of large droplets, the smallest resolved structures. At the same time, smaller liquid structures detach from the thinner surface ligaments, which would form the first population of small droplets in the actual jet.

As the LES/multi-fluid method is not designed to capture the smallest droplets, the solution of the ligaments breakup appears as a diffuse zone except for the largest ones: in these zones, the liquid volume fraction is small and no interface can be captured anymore. These regions are specifically the ones that the proposed model aims to characterize through the reconstruction of a characteristic liquid length scale, given by the ISD model.

2.3. Model validation strategy

The validation of the model will be performed against the data available from the DNS of Hoarau et al. [16]. To compare the model and the DNS, the LES simulation is realized on the same geometry and with the same boundary conditions. The domain is only shorter than the DNS, as the spray downstream of the atomization zone is not the focus of this study. In particular, the mesh refinement is identical within the injector for the LES cases defined in Section 2.2. To confirm this, Figure 4 presents the gas and liquid mean velocity profiles at injection, $X = 0$. As observed, the LES and DNS profiles are very closely matched, with only a slight difference in the external radius of

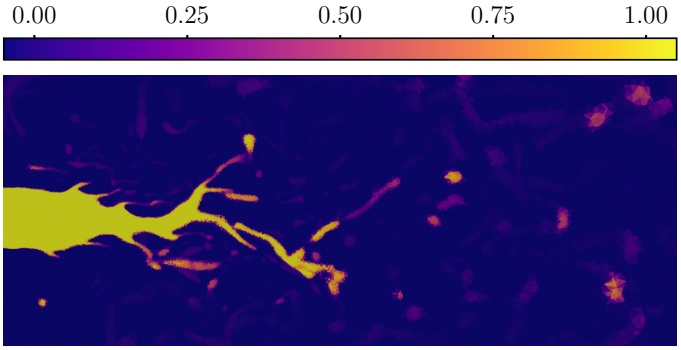

Figure 3: Instantaneous liquid volume fraction field on LES-M9

the gas injector. This difference is not significant as the atomization process occurs at inner radius positions, where the LES gas velocity profiles align with those of the DNS. No turbulence was added to the injection boundary conditions in either simulation.

It is worth noting that the interface capturing method involved in Hoarau et al. [16] better estimates (not shown here) interface area density than the LES/multi-fluid method used in this paper, but it remains influenced by the mesh size. This effect on DNS results is not addressed in this paper, and we used the most accurate DNS results as reference to validate the model proposed in the following section.

3. Model formulation

This section presents a new IAD model adapted for LES of assisted atomization, inspired by the work of Chesnel et al. [34]. The model decomposes the IAD Σ into two parts, namely a resolved $[\cdot]_{\text{res}}$ and a sub-grid $[\cdot]'$ part, similar to the decomposition used for turbulence modeling:

$$\Sigma = \Sigma_{\text{res}} + \Sigma' \,. \tag{17}$$

The resolved part of the ISD, Σ_{res}, is computed by the separate phases solver, in this case the multi-fluid described in Section 2.1. The interfacial model is a diffuse interface, in which the interface is "captured" by smooth variations of the local volume fractions. In order to get consistent and accurate values for liquid structures surface, the liquid volume fraction α_l was taken as a smoothed Heaviside function. In consequence, its derivative can be used as a smoothed Dirac function describing the discrete interface. The definition for the resolved interface area density is therefore based on the gradient of the liquid volume fraction as:

$$\Sigma_{\text{res}} = \|\nabla \alpha_l\| \,. \tag{18}$$

This definition allows the computation of the actual surface of a liquid structure, and gives results accurate up to $\approx 1\%$ on a structure described by the full range of volume fraction, i.e. $0 \leq \alpha_l \leq 1$. This means that the resolved surface density accounts for all the large scale resolved liquid structures surface, such as the liquid core.

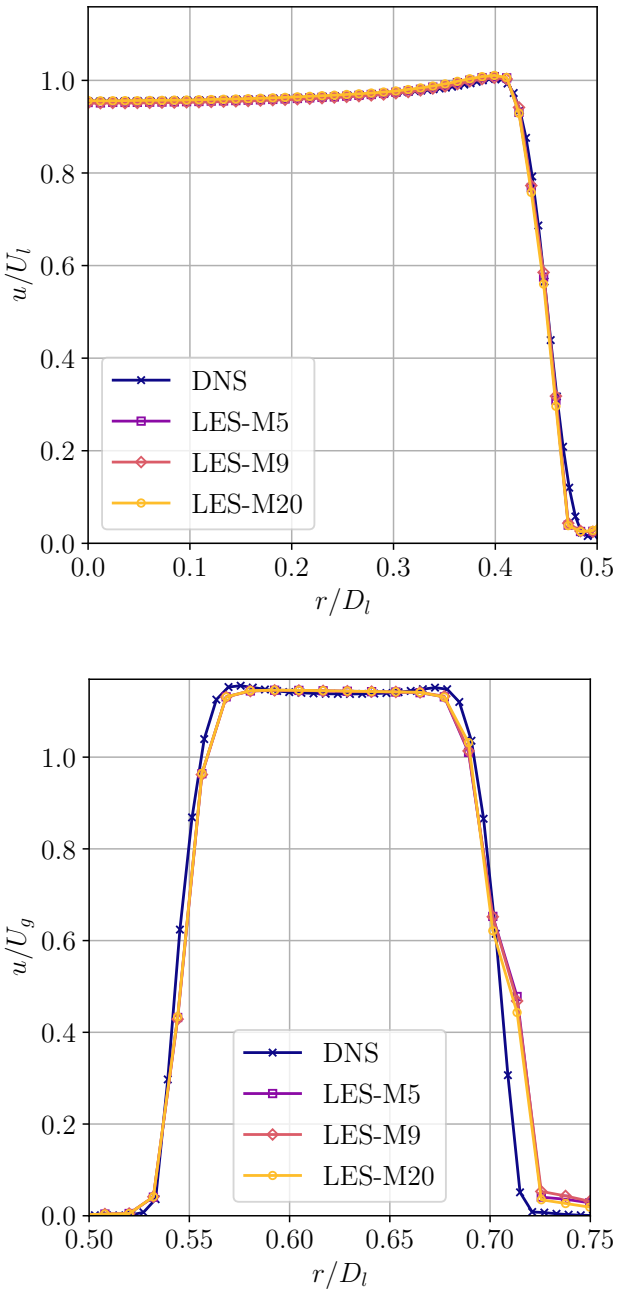

Figure 4: Liquid (top) and gas (bottom) injection mean velocities at $X = 0$ for DNS and LES

The IAD sub-grid part obeys an advection-diffusion equation:

$$\frac{\partial \Sigma'}{\partial t} + \frac{\partial \widetilde{u_i} \Sigma'}{\partial x_i} = \frac{\partial}{\partial x_i}\left(D_s \frac{\partial \Sigma'}{\partial x_i}\right) + \dot{\Sigma}_p \,. \tag{19}$$

Similar to the approach presented by [34], the diffusive term, the first term on the right-hand side of Equation 19, is modeled like a turbulent diffusion mechanism, with a turbulent diffusion coefficient D_S. This coefficient is chosen the same as the one of the turbulence model employed for closing the momentum equation. $\dot{\Sigma}_p$ is the source term of interface production

defined as an equilibrium relaxation term tending to an equilibrium value, in which the atomization is finished:

$$\dot{\Sigma}_p = f_{\text{atom}} \times \lambda_{\text{atom}} \times \Sigma \times \max\left\{\left(1 - \frac{\Sigma}{\Sigma_{\text{cr}}}\right), 0\right\} \times \Psi \,. \tag{20}$$

The production source term $\dot{\Sigma}_p$ relies on several terms including the characteristic frequency of IAD creation f_{atom}, an atomization location term λ_{atom}, a mesh convergence term Ψ, and the critical value of interface area density Σ_{cr}. The detailed definition of these terms will be given in the subsequent sections.

3.1. Atomization frequency

The characteristic time of the interface area density is a key parameter, written as a frequency is denoted as f_{atom}, and used in Equation 20 to describe the rate at which Σ approaches its equilibrium value. Unlike the characteristic time used for diesel jet atomization in Equation 10, which is related to turbulence through the strain tensor S, the characteristic time for assisted atomization depends on the relative velocity between the gas and the liquid $|u_g - u_l|$. A dimensionless characteristic frequency of drop breakup by Rayleigh-Taylor or Kelvin-Helmholtz instabilities, proposed by Pilch and Erdman [44], is used to define this characteristic time:

$$f^* = \frac{|u_g - u_l|}{d_{\text{min}}} \left(\frac{\rho}{\rho_l}\right)^{0.5} \,, \tag{21}$$

with d_{min} a characteristic diameter detailed below, ρ the local density, ρ_l the liquid density and $|u_g - u_l|$ the liquid/gas relative velocity which requires a closure (Section 4) for the two-phase modeling defined in Section 2.1. Although Equation 21 provides a dimensionless characteristic frequency of drop breakup, it does not directly represent the timescale for interface creation and requires a more detailed analysis of the breakup phenomena. As noted by Hoarau et al. [16], the maximum creation of interface area density is located in regions with ligaments both attached to the liquid core and detached from it. This suggests that the characteristic time for interface area density is related to the initiation of breakup described by Pilch and Erdman [44] as:

$$f^*/f_{\text{atom}} = 1.9(\text{We}_{\text{local}} - 12)^{-0.25}(1 + 2.2\ \text{Oh}^{1.6}) \,, \tag{22}$$

with We_{local} the local Weber number, that relies on a local characteristic length defined with the local Σ value as in Equation 23:

$$\text{We}_{\text{local}} = \frac{\rho(u_g - u_l)^2}{\sigma\Sigma} \,, \tag{23}$$

and the Ohnesorge number that describes the deformation of liquid structures as in Equation 24 by relating viscous forces to surface tension and inertial forces:

$$\text{Oh} = \frac{\mu_l}{(\rho_l L \sigma)^{0.5}} \,. \tag{24}$$

For the configuration studied, Marmottant and Villermaux [5] predict an average atomized drop diameter of $0.55\,\delta_{\text{lip}}$, resulting in Oh $\sim$ 0.01. A small Ohnesorge number indicates that surface tension and inertial forces dominate over viscosity, resulting in low-viscosity drops.

3.2. Critical Weber number

The critical value Σ_{cr} represents the maximum quantity of IAD attainable in a given configuration. Similar to the IAD, Σ_{cr} can also be decomposed into a resolved part $[\cdot]_{\text{res}}$ and a fluctuating part $[\cdot]'$, following the same method as described in Equation 17:

$$\Sigma_{\text{cr}} = \Sigma_{\text{res}} + \Sigma'_{\text{cr}} \,, \tag{25}$$

with Σ'_{cr} the sub-grid part of the interface area density critical value. Σ'_{cr} contains all the physics of IAD creation, including primary breakup and coalescence. In assisted atomization, the relative velocity between the gas and the liquid is crucial for interface creation, and this needs to be accounted for in the modeling of Σ'_{cr}. To close the Σ'_{cr} term, Chesnel et al. [34] use the critical Weber number given in Equation 8. Pilch and Erdman [44] give an experimental correlation for the critical Weber value of droplets. It depends on the Ohnesorge number and is defined in Equation 26:

$$\text{We}_{\text{cr}} = 12\left(1 + 1.077\,\text{Oh}^{1.6}\right) \,. \tag{26}$$

Using the Ohnesorge number previously determined for the configuration studied, Equation 26 gives $\text{We}_{\text{cr}} \sim 12$ in a laminar flow. As the atomization process creates structures of various shapes, including elongated ligaments that are necessarily less stable than droplets, the critical Weber number is expected to be lower than 12 but higher than $\text{We}_{\text{cr}} = 1.18$ given by Hinze [45] for droplets in a flow dominated by turbulence. The value for this configuration is provided in Section 5. Using a We_{cr} within this range, the maximum stable diameter of atomized droplets definition from Pilch and Erdman [44] is extended to liquid structures of general shapes and is identified as $1/\Sigma'_{\text{cr}}$ in this paper:

$$\Sigma'_{\text{cr}} = \frac{\rho(u_g - u_l)^2}{\sigma\,\text{We}_{\text{cr}}} \times \left(1 - \frac{v_{\text{drop}}}{|u_g - u_l|}\right)^2 \,, \tag{27}$$

with v_{drop} the velocity of liquid structures that just detached from the main liquid core, further referred to as the atomization velocity. Equation 27 points out that the atomization velocity modeling directly influences the interface creation. A slower atomization velocity would result in a larger interface area as the structure could be deformed or broken up by the gas. In contrast, a higher atomization velocity would result in a smaller IAD creation as liquid structures would be closer to the equilibrium. This paper assumes that droplets are atomized at a velocity equal to the local liquid velocity. By injecting $v_{\text{drop}} = u_l$ into Equation 27, the sub-grid critical value of IAD becomes:

$$\Sigma'_{\text{cr}} = \frac{\rho(u_g - 2u_l)^2}{\sigma\,\text{We}_{\text{cr}}} \,. \tag{28}$$

Equation 28 differs from the traditional Weber number formulations that depend on ΔV. An interpretation of this difference is that, by choosing the initial droplet velocity as the local velocity, the atomization process occurs only when $u_g > 2u_l$. Otherwise, no fragmentation of the structure happens as the relative velocity is not sufficient to break the liquid structure. The local drop diameter is then defined by solving Equation 28 for the characteristic length:

$$d_{\min} = \frac{1}{\Sigma'_{\text{cr}}} = \text{We}_{\text{cr}} \frac{\sigma}{\rho |u_g - 2u_l|^2} , \tag{29}$$

where $d_{\min}$ is the diameter that describes the size of the smallest possible atomized structures and will be further used in the model.

3.3. Atomization location

Assuming that the assisted atomization process is solely driven by the relative velocity between the liquid and the gas is not sufficient to accurately model the IAD creation. As described in Hoarau et al. [16], the atomization process does not occur right after the liquid comes out from the injector despite having the highest relative velocity with the gas flow. In fact, it takes time for the Rayleigh and Plateau instabilities to grow and finally create interface through ligaments. In other words, without any additional term, the model would predict IAD creation right out of the injector, which is not consistent with observations [16]. Therefore, an additional term λ_{atom} is required in Equation 20 to delay the IAD creation in the chamber and is defined as an indicator function ($\mathbb{R} \longrightarrow [0, 1]$):

$$\lambda_{\text{atom}}(X) = \frac{1}{1 + exp(-b_\lambda (X - a_\lambda))} . \tag{30}$$

b_λ characterizes the slope of the λ_{atom} function and a_λ is the position for which $\lambda_{\text{atom}} = 0.5$. The purpose of the λ_{atom} function is to be equal to 1 downstream of the atomization zone and 0 upstream. The value of a_λ is then determined by imposing a value close to 1 (0.9 in this section) at the atomization startup position X_{atom}. An estimation of the average breakup length X_{atom} was obtained by the results of the DNS. This length is given by the position of the average volume fraction $\alpha_l = 0.5$ iso-contour, and corresponds to the maximum IAD production location as per [16]. This leads to a coefficient $a_\lambda = 1.70$, which will be used in subsequent parts of this study together with b_λ fixed to 5.

A sensitivity analysis of these parameters is conducted in Appendix A. The results suggested an strong influence of the length scale (parameter a_λ), and a very limited influence of the function shape (parameter b_λ). In the proposed paper, the coefficient a_λ was expressly "tuned" on the DNS results, so that the λ_{atom} gives the good length scale for triggering ISD generation. This value may need further tuning when confronted to different atomization regimes. On the other hand, the physical quantity involved may be easily recovered using a local, more refined preliminary simulation, available experimental data, or correlations on the characteristic development time of the ligaments.

3.4. Mesh dependence

One notable distinction from the modeling approach presented in [34] is that the sub-grid critical IAD Σ'_{cr} does not depend on modeled sub-grid quantities, but it relies on resolved field quantities. This implies that i) the resolution of the dense phase model has a direct influence on this term, and ii) the model must activate only where a local under-resolution of the two-phase dense solution is detected. In other words, the coupled LES and IAD model should rebuild the missing scales for a large range of LES mesh sizes, but it should degenerate towards a model-less DNS under unrestricted mesh refinement.

To recover mesh independence of this term, an extra term Ψ was included in Equation 20. The formulation of Ψ requires an estimation of the smallest possible liquid structure scales, which has been defined as $d_{\min}$ in Equation 29. Indeed, the model should then be aware of the difference between the smallest resolved scales the LES can simulate, and the actual expected smallest liquid scales in the flow.

A reconstructed interface approach has been shown to accurately resolve the smallest structures up to 2Δ in [16], whereas this number is expected to be higher with a diffuse interface model. In this paper, the resolution criterion is based on the measurement of the liquid structure's interface area A. This area is equal to the integral of the volume fraction gradient, or Σ_{res} (Equation 18):

$$\text{A} = \int \Sigma_{\text{res}} . \tag{31}$$

If a liquid structure contains cells with $\alpha_l = 1$, Equation 31 gives the actual liquid structure interface area. To characterize the resolution of the diffuse interface model used in this paper, deep analysis of results of a spray simulation on a very fine mesh, not shown in this paper for the reason of conciseness, showed that most liquid structures whose size is $D_{30} > 5\Delta$ contain one or more cells with $\alpha_l = 1$. That indicated that Equation 31 could accurately retrieve these structures' interface area with the gradient of the liquid volume fraction. Taking this condition as a resolution criterion, we propose to express the Ψ function as follows:

$$\Psi(d_{\min}, \Delta) = \begin{cases} 1 - \dfrac{d_{\min}}{5\Delta} & \text{if} \quad 5\Delta > d_{\min} , \\ 0 & \text{otherwise} . \end{cases} \tag{32}$$

$\Psi : \left(\mathbb{R}_0^+\right)^2 \longrightarrow [0, 1]$ is the resolution indicator function, whose shape is chosen arbitrarily here. In cells with a characteristic size smaller than the smallest two-phase flow scales, $\Psi \rightarrow 0$, deactivating the IAD model. Conversely, if the cell size is much larger than the smallest two-phase flow scale, then $\Psi \rightarrow 1$. The Ψ function is plotted in Figure 5 for a range of cell size that would be encountered in a practical mesh from 0 µm to 500 µm for four $d_{\min}$ values from 10 µm to 200 µm.

4. Prediction of velocity profiles

The main challenge in the presented IAD model lies in accurately estimating the gas and liquid velocities (u_g and u_l) involved in the definition of Weber numbers, in Equation 23,

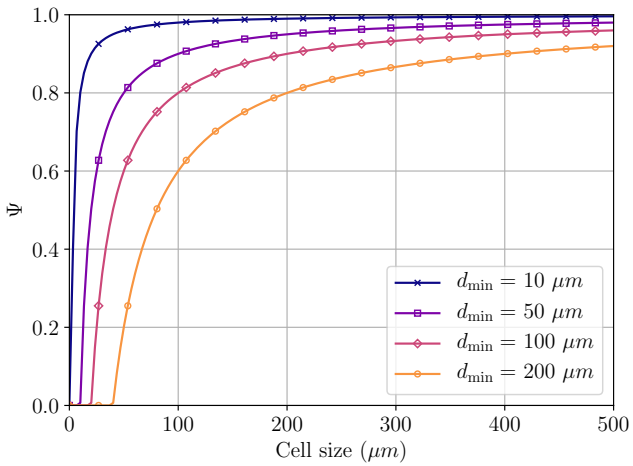

Figure 5: Resolution indicator function Ψ

Equation 28 and Equation 29. Indeed, estimations of a critical Weber number are usually given for an isolated liquid structure of velocity u_l immersed into an unperturbed uniform gas stream of velocity u_g [46]. In particular, in the 4-equations diffuse interface model used in this study, a local equilibrium hypothesis is made, i.e. the local cell velocity denoted as u is the same for both fluids $u = u_g = u_l$. To estimate the liquid velocity, Blanchard [47] showed that the velocity u could be a good approximation of the liquid velocity in cells containing both liquid and gas if the liquid density ρ_l significantly exceeds the gas density ρ_g. This condition, considered satisfied for $\alpha_l \gg 10^{-3}$, is verified for most cells in the liquid core interface, where the IAD model is actively applied.

To determine the gas velocity u_g responsible for the local breakup, and thus driving the atomization model, one possible approach is to use the gas injection velocity U_g to estimate the local Weber number of a liquid structure. This approach would yield accurate values of the local Weber number near the back plate, where the gas velocity is similar to the injection velocity. However, this approach would lead to an overestimation of the Weber number in the atomization zone due to the rapid deceleration of the gas caused by the expansion of the jet in the chamber and the friction with the liquid. This paper proposes an alternative method to estimate the gas velocity in a coaxial injector based on free jet considerations. By employing this approach, detailed below, a more accurate estimation of the gas velocity in the atomization zone can be obtained.

4.1. Velocity decay in free jets

The study conducted by Malmström et al. [48] presented experimental data on velocity decay and transverse velocity profiles of an axisymmetric jet. The decay of centerline velocity is modeled using a simple $1/x$ law:

$$\frac{u_{\text{axis}}(x)}{U_{\text{inj}}} = K\frac{D_{\text{inj}}}{x}\,, \tag{33}$$

with U_{inj} the injection velocity, $u_{\text{axis}}(x)$ the centerline mean velocity, D_{inj} the injection diameter and a velocity decay coefficient K. The radial velocity profiles are determined under the self-similarity hypothesis by the following law:

$$\frac{u(x,\eta)}{u_{\text{axis}}(x)} = e^{-\ln(2)\eta^2}\,, \tag{34}$$

where $u(x,\eta)$ is the mean velocity at the distance x from the backplate at a non-dimensional transverse coordinate $\eta = r/r_{0.5}$ (also known as similarity parameter), with r the distance to the jet axis and $r_{0.5}$ the radius where $u(x,1)/u_{\text{axis}}(x) = 0.5$. The laws (33) and (34) were extended by Awbi [49] to various non-circular free jets configurations. For instance, in the case of plane jets, which are infinitely long rectangular injectors, the decay law follows a $1/\sqrt{x}$ decrease. It is worth noting that Malmström et al. [48] demonstrated that the decay coefficient K remains independent of the injection conditions U_{inj} and D_{inj}.

4.2. Gas velocity decay in coaxial jets

To evaluate a velocity decay law in a coaxial liquid-gas jet, two gas velocity decay laws $u_{g,\max}$ adapted from round ($[\cdot]_{rnd}$) and plane ($[\cdot]_{pla}$) free jets [49] are fitted to the gas velocity decay from the DNS data:

$$u_{g,\max,\text{rnd}} = u_\infty + U_g \times K \times h_g/x\,, \tag{35}$$

and

$$u_{g,\max,\text{pla}} = u_\infty + U_g \times K \times (h_g/x)^{0.5}\,. \tag{36}$$

To ensure a non-zero value for the gas velocity in the far field, a constant u_∞ is added to the fitted functions, showing improved results. The coefficients u_∞ and K obtained for the given coaxial configuration are provided in Table 3. These coefficients are specific to the coaxial geometry and differ from those found for plane and free jet configurations, as the geometry of the coaxial setup is significantly different with the presence of a liquid jet. Both fitted functions, with the parameters provided in Table 3, exhibit excellent agreement with the gas velocity decay as shown on Figure 6.

Some small differences are observed, particularly in the region between 1.5 and 7.5 D_l. The differences for the $\sqrt{1/x}$ fitted function appear to be more significant in the region between 1.5 and 5.0 D_l. On the other hand, the $1/x$ fitted function shows good agreement in this zone but exhibits differences with the DNS data between 3 and 7.5 D_l. Since the atomization process begins at 1.5 D_l and reaches its maximum at 2.5 D_l [16], the choice is made to use the $1/x$ velocity decay function as it better fits this zone. It should be noted that the $1/x$ fitted function slightly overestimates the gas velocity in the far field, which is not a problem since the production of interface area density is concentrated between 1.5 and 3.0 D_l.

4.3. Undeflected gas velocity

The gas velocity is reconstructed throughout the domain by employing the $1/x$ decay law from Equation 35 and assuming the auto-similarity of the velocity profiles. This gas velocity reconstruction is performed without considering the presence of

	Round [48]	Plane [50]	Coaxial $1/x$	Coaxial $1/\sqrt{x}$
u_∞ $(m.s^{-1})$	0	0	1.15	−3.46
K	[5.8 : 6.0]	[2.5 : 3.5]	3.70	1.93

Table 3: Decay laws K and u_∞ coefficients from cylindrical, plane laws and fitted functions for coaxial gas jets

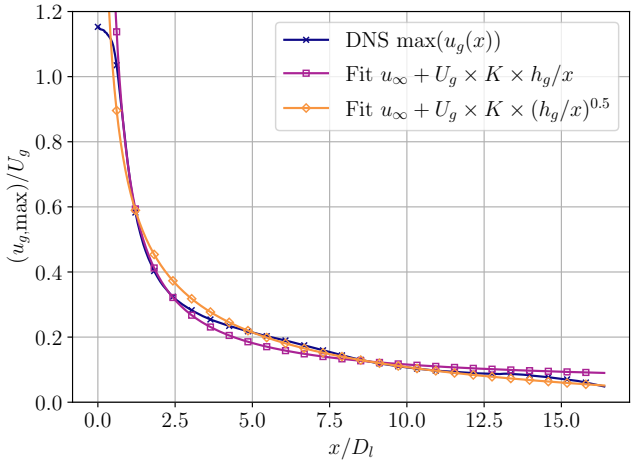

Figure 6: Gas velocity decay with fitted functions

the liquid on the inner radius, making it equivalent to the undeflected gas velocity, as seen by the liquid during the atomization process, and denoted as $u_{g,rec}$ at any position x and η:

$$u_{g,\mathrm{rec}}(x,\eta) = e^{-\ln(2)\eta^2} \times \left(u_\infty + U_g \times K \times h_g/x\right) . \tag{37}$$

Assuming that the local velocity u is equal to the liquid velocity u_l and reconstructing the undeflected gas velocity $u_{g,\mathrm{rec}}$ based on free jet considerations, the relative velocity ΔV_{rec} used in the following sections of the paper, for the IAD model presented in Section 3, is given by:

$$\Delta V_{\mathrm{rec}} = u_{g,\mathrm{rec}} - u \tag{38}$$

The presented velocity decay law has been fitted to the DNS data in the current work. However, its closure is not expected to need adjustments for different regimes in the coaxial configuration. This hypothesis will need further testing and validation in future work.

5. IAD model validation

The following section focuses on validating the proposed numerical strategy for an LES simulation of the coaxial jet assisted atomization. The validation will be performed against the results of a DNS from [16]. The full numerical model consists of Equation 19 and Equation 20 coupled to the multi-fluid model presented in Section 3 and consisting of the Equation 12. The simulation is carried on the LES-M9 mesh presented in Section 2.2 in the same conditions as the DNS (see Table 1), in a domain of size $\{Lx,\ Ly,\ Lz\} = \{11\,\mathrm{D_l},\ 6\,\mathrm{D_l},\ 6\,\mathrm{D_l}\}$.

The simulation was carried out for 36 ms physical time, close to the 30 ms for the DNS, allowing for full development of the primary atomization and convergence of the resolved/sub-grid interface area density fields.

5.1. Qualitative observations

Instantaneous cut fields in a plane perpendicular to the Z-axis, passing through the injection axis, can be seen Figure 7. The radius range extends from $-1.0\,\mathrm{D_l}$ to $1.0\,\mathrm{D_l}$ and covers the region from the back-plate to $X = 10\,\mathrm{D_l}$. The represented fields are the liquid volume fraction α_l, the resolved, sub-grid and total components of the IAD from Equation 18 and Equation 19. The instantaneous α_l field shows the section of the perturbed continuous liquid core and several detached liquid structures. It can be seen that the dense model on the current mesh is able to resolve the main liquid jet and its deformations, but it cannot resolve the smaller structures as the liquid is advected downstream, which are more and more diffused as the physics of atomization takes place and reduces the local structure size. The corresponding field of resolved IAD (in logarithmic scale) clearly shows the boundaries of the main liquid structures. Still, of course, it cannot recover the interface area of the unresolved liquid structures. It is on these under-resolved zones that the model activates, generating sub-grid interface area density. A notable distinction between the Σ_{res} and Σ' fields is that Σ_{res} is located on the outer boundary of the interface where liquid volume fraction is low, while the sub-grid IAD Σ' is also generated at higher liquid volume fractions. This characteristic arises from the diffuse interface modeling and would not be observed in methods employing sharp interface representations.

5.2. Liquid core validation

As stated in Section 2, the DNS results allow for a direct comparison of the LES and model outputs. To compare the results of the two simulations, time averages were performed on all the available time steps (except the initial transient), and azimuthal spatial averages were performed, assuming that the flow is mainly axisymmetric. The first quantitative validation is performed on the liquid field resolved by the dense phase solver. As visible in Figure 7 (a), the dense phase method can capture the continuous liquid jet extending to some 2−3 diameters from the injection. An estimation of the liquid breakup length, or intact core length, can be obtained from the average liquid phase function: a comparison of the average liquid volume fraction

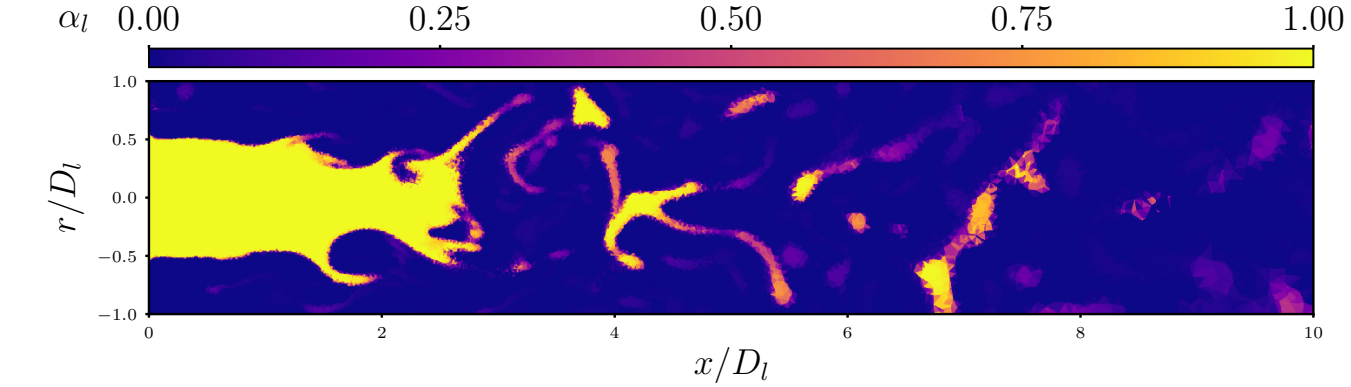

(a)

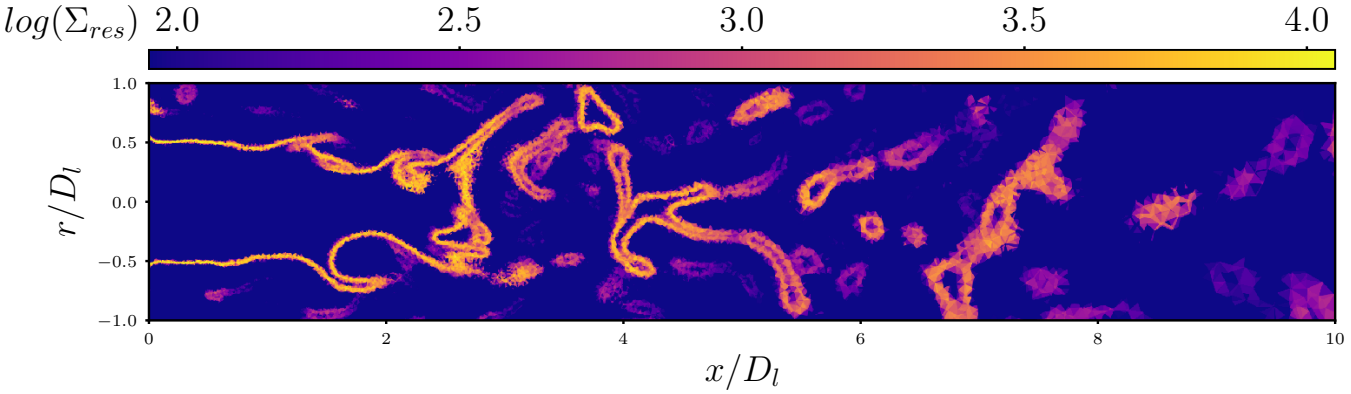

(b)

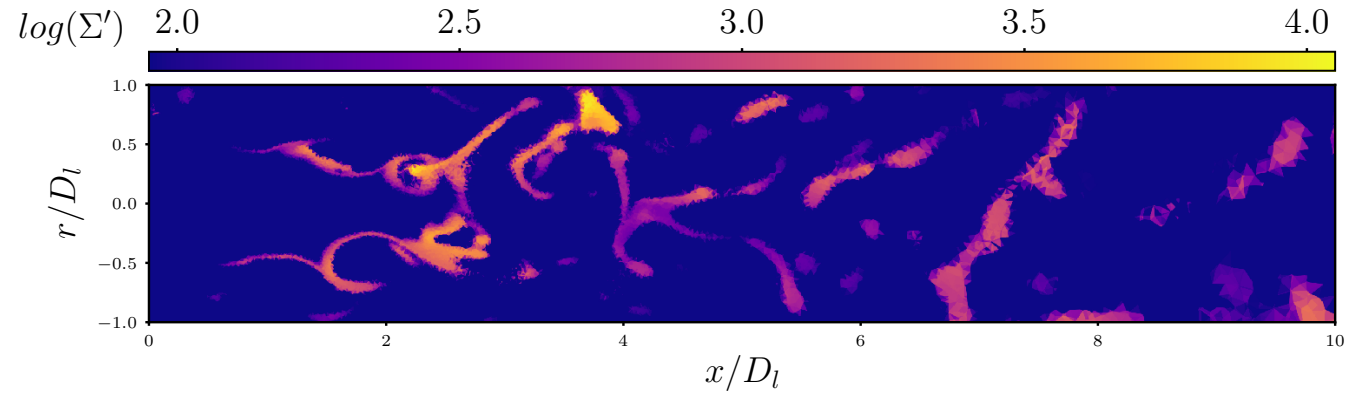

(c)

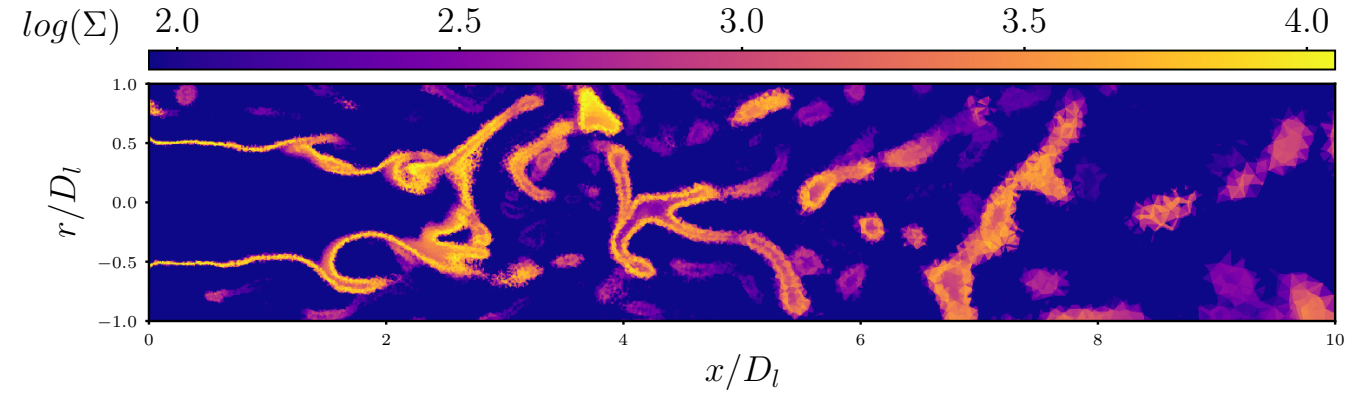

(d)

Figure 7: Instantaneous fields from LES using the IAD model. (a) Liquid volume fraction α_l, (b) resolved IAD Σ_{res}, (c) sub-grid IAD Σ' and (d) total IAD $\Sigma = \Sigma_{res} + \Sigma'$

of the LES and the DNS is presented in Figure 8, for both the $\alpha_l = 1$ and $\alpha_l = 0.5$. The DNS results show a shorter breakup length with both iso-contours, respectively at about 1.5 D_l and 2.2 D_l. Conversely, the diffuse interface model predicts around 1.8 D_l for the first one and more than 3.2 D_l for the second one: this result can be expected, as the sharp interface model and the finer mesh of the DNS allow for faster development of the interfacial instabilities. From this result, an atomization delay is expected from the LES simulation.

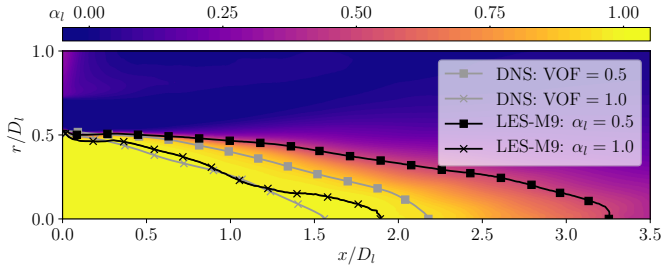

Figure 8: Liquid core length comparison between LES-M9 mesh and DNS

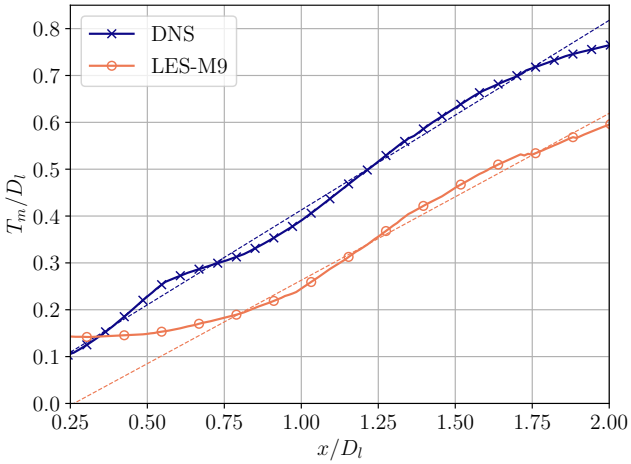

Figure 9: Mixing layer thickness evolution for both LES and DNS

5.3. Mixing layer validation

To better understand this behavior, which may affect the effectiveness of the atomization model, the mixing layer thickness is investigated near the injection zone as a key quantity for assisted atomization. The mixing layer evolution involves the momentum exchange between the two streams and is affected by the difference in velocity and density of the two fluids. To calculate the mixing layer thickness, the radial distance between the positions of 99% of the maximum liquid and gas velocities on the time-averaged fields is measured. The results for the DNS and LES-M9 cases are shown in Figure 9, along with the corresponding linear regressions indicated by dashed lines. The growth of the mixing layer thickness exhibits a linear trend, highlighted by the regression lines.

As anticipated, the DNS consistently exhibits a thicker mixing layer than LES-M9 at the same streamwise location. Indeed, the LES thickness remains almost unchanged up to 0.5 D_l from the backplate, while the linear behavior starts from 0.25 D_l in the DNS. The LES thickness behavior becomes linear as well from about 1 D_l, and it is interesting to see that the rate of expansion is very similar to the DNS: in other words, the mixing layer development is similar, but delayed by a constant of less than one diameter in the present simulation. This can be attributed to the filtering effect in LES, which delays the growth of vortices and the increase of the mixing layer thickness.

5.4. Interface area density validation

Figure 10 shows time and azimuthal average radial profiles of interface area density for both LES-M9 and DNSs at different streamwise locations $X = \{1, 2, 3, 4\}$ D_l. The comparison with the DNS results is satisfactory, but the LES IAD field appears shifted toward the azimuthal direction compared to DNS. As shown in Section 5.2 and Section 5.3, the development of the two-phase flow in terms of liquid core and mixing layer presents a spatial delay of about 0.75 D_l for the LES. In consequence, in Figure 11 and in all the following, the DNS profiles are compared to the LES ones located at a streamwise distance corrected by this offset, i.e. $X_{\text{LES}} = X_{\text{DNS}} + \text{offset}$, this offset being almost constant for the whole considered range of distances. Using this offset clearly improves the match between the total Σ over the DNS reference.

On Figure 11, the LES profiles are split into resolved interface area density Σ_{res} (from Equation 18), the model predicted Σ (from Equation 19) and their sum Σ. Figure 11 (a) shows the profiles at one diameter from the backplate. Near the centerline, the DNS predicts almost zero interface area as this location is occupied by the round jet. A small increase in Σ_{res} indicates the presence of a diffuse interface, whose thickness increases with the distance. A peak in the DNS and Σ_{res} is visible near 0.5 D_l, indicating a strong two-phase interaction and interface area production. In this zone, the model adds a small quantity of Σ', which complements well the resolved one: the total Σ is almost superposed to the DNS values. A steep decrease of all the curves farther from the axis indicates a zone mostly occupied by gas only.

One diameter downstream, on Figure 11 (b), the DNS curve shows a larger peak but larger, as liquid deformation and detached structures are generated by primary atomization. The resolved Σ_{res} shows a similar behavior but with increasing magnitude, again with the modeled Σ' allowing the total interface area to match the DNS result. Interestingly, the model is able to correctly capture the small scales which make almost all the IAD for $R = r/D_l < 0.5$ D_l, while for $R > 0.5$ D_l the resolved and modeled values contribute equally to the total area. A small spike is observed at $R = 1.3$ D_l, corresponding to accumulated liquid in the recirculation zone that gets atomized by the gas co-flow just out from the injector and is not observed on the DNS.

At $X_{\text{DNS}} = 3$ D_l, Figure 11 (c) shows more diffused profiles.

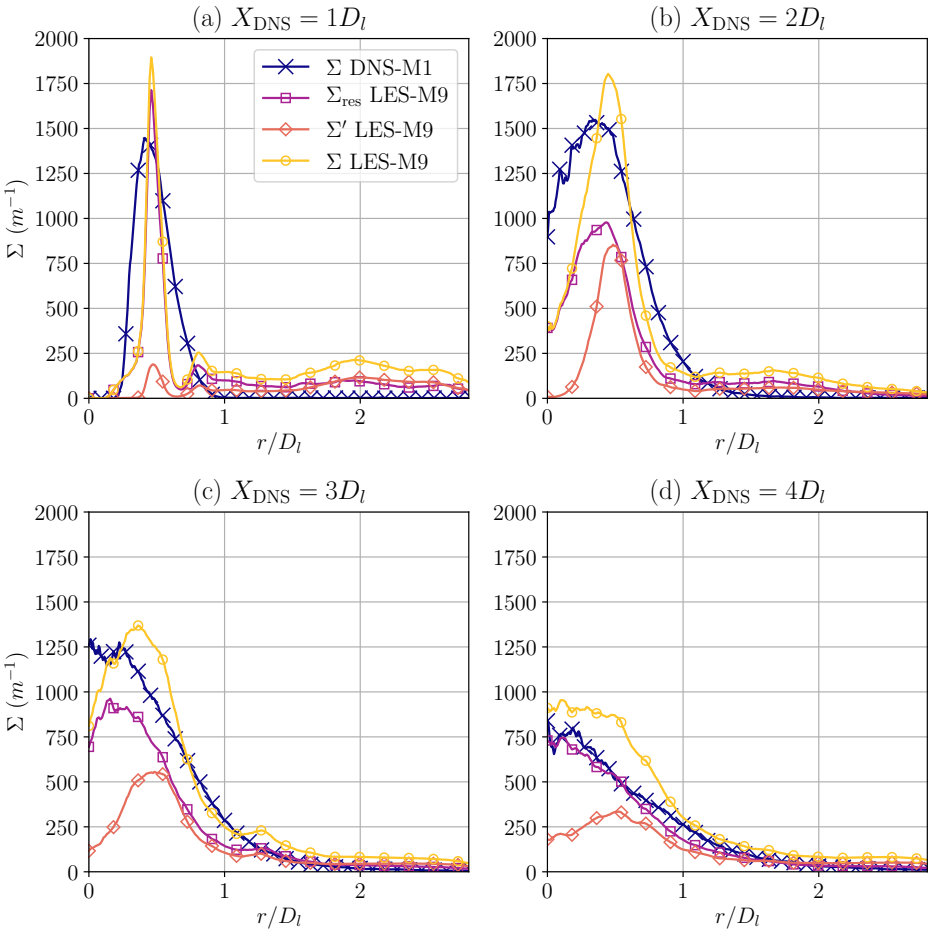

Figure 10: Interface area density profiles at positions $X = 1, 2, 3, 4\,\mathrm{D_l}$ for the DNS and the LES with the IAD model of this paper at $\mathrm{We_{cr}} = 3.5$

For $R < 0.4\,\mathrm{D_l}$, the total LES IAD is slightly underestimated, while it continues to match very well the DNS one up to $R = 1$. At larger radial distances, there seems to be a small overestimation given by the presence of modeled Σ' summing up to an already matching Σ_{res}.

Finally, Figure 11 (d) exhibits similar results to Figure 11 (c); however, the slight overestimation observed far from the injection axis is now present across all radii. This highlights a limitation of the current formulation, which focuses solely on the mechanisms of interface creation and does not account for those of interface destruction.

Overall, the results obtained by the LES plus IAD model are very satisfying, given the difficulty of the task and the number of terms playing a role in the relatively simple modeling of Equation 19. To increase the confidence in the model, a study on its sensitivity to the most relevant parameters and the LES mesh size was conducted. The results are presented in the next section.

6. Mesh convergence and model sensibility

6.1. Mesh convergence

The proposed numerical method works assuming that the dense phase model and the IAD model can respectively deal with the large two-phase scales of the flow and the sub-grid scales, mostly corresponding to the dispersed phase. The primary filter, which splits the large and small scales, is the LES mesh size. Ideally, an unrestricted mesh refinement would lead the dense phase model to provide a DNS-accurate solution of the flow, where Σ_{res} IAD accounts for the total interface area; conversely, a very coarse mesh would give a very badly resolved interface area, forcing the model to reconstruct small and large scales. In practice, there is no proof that the diffuse interface model would converge to the DNS solution; however, convergence on the resolved large scales together with the expected behavior of the model would be sufficient to rebuild a good approximation of the liquid interface area density.

The main assumption made in the building of the model is that the dense phase solver is able to solve at least the largest scales involved in the jet's primary atomization, such as the intact liquid jet, its interface surface waves, and the largest liga-

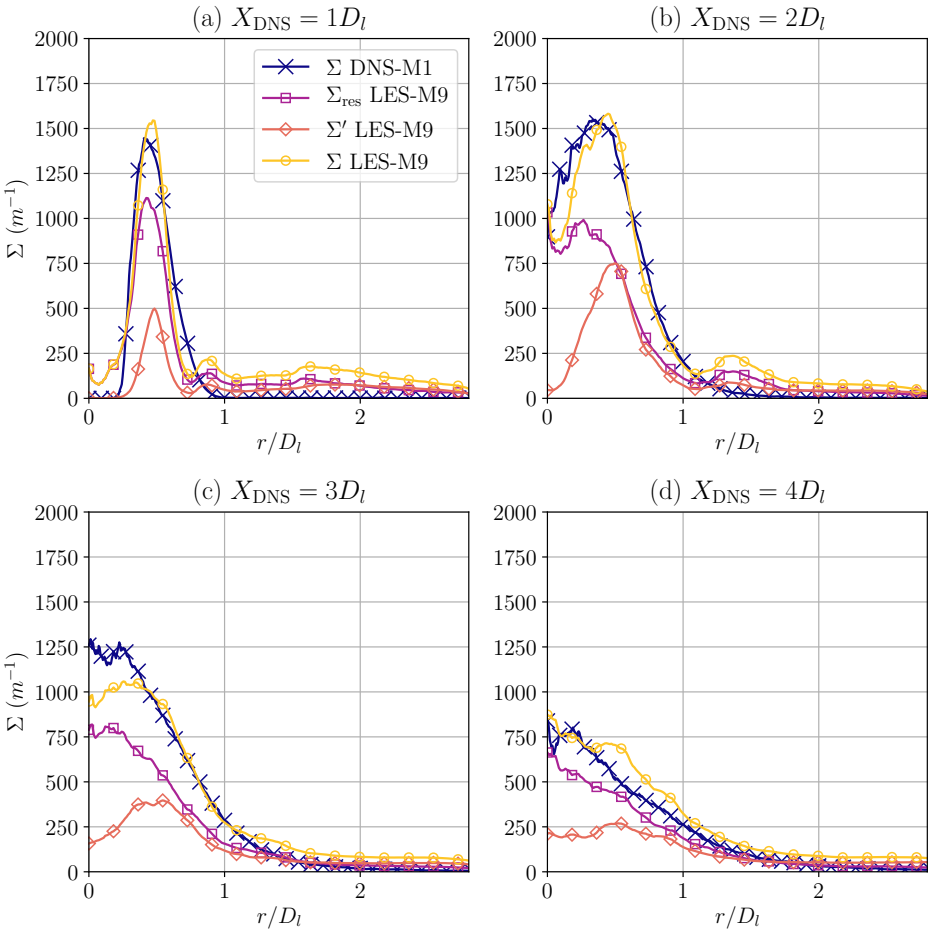

Figure 11: Interface area density profiles at positions $X_{\mathrm{DNS}} = 1, 2, 3, 4\,\mathrm{D_l}$ for the DNS and at corresponding positions corrected by the offset for the LES with the IAD model of this paper at $\mathrm{We_{cr}} = 3.5$

ments (see Figure 3 and Figure 7 (a)). This solution gives the model appropriate local data, such as the liquid velocity. It is evident that different LES mesh resolutions would change the quality of the dense phase solution and the relative model contribution.

Several simulations with different LES mesh resolutions were carried out to characterize this effect better, keeping the same $\mathrm{We_{cr}}$, and compared in terms of IAD to the reference DNS. Figure 12 shows the same IAD time and space averaged radial profiles at different streamwise positions for the DNS and the three meshes described in Section 2.2. The plots show an excellent agreement of the total IAD for the three LES meshes M5, M9 and M20, showing the capability of the model to adapt to the local dense phase resolution, adapting the balance. Some differences can be seen at the very initial peak at $X_{\mathrm{DNS}} = 1\,\mathrm{D_l}$, and downstream at $X_{\mathrm{DNS}} = 4\,\mathrm{D_l}$. To further assess the behavior of the model as a function of spatial resolution, the ratio of modeled IAD to total IAD is compared in Figure 13. Here, it can be seen that the modeled part of the IAD decreases with mesh refinement. This confirms the good trend of the model, which generates decreasing sub-mesh IAD as the mesh is refined.

6.2. *Critical Weber Number*

The critical Weber number described in Section 3.2 plays a key role in the evaluation of the local smallest allowable liquid scale Σ'_{cr}, defined in Equation 28. In consequence, the sensitivity of the IAD model to the choice of the critical Weber number is investigated in this section. The IAD profiles obtained from LES simulations with different values of $\mathrm{We_{cr}} = \{1, 3, 4, 5, 7\}$ are compared to the DNS Σ profiles at positions $X_{\mathrm{DNS}} = \{1, 2, 3, 4\}\ \mathrm{D_l}$ in Figure 14. This analysis aims to assess the impact of varying $\mathrm{We_{cr}}$ on the accuracy of the IAD predictions.

The IAD model with $\mathrm{We_{cr}} = \{3, 4, 5, 7\}$ shows a good agreement with the DNS results in this configuration. As expected, a higher $\mathrm{We_{cr}}$ leads to lower values of Σ on average. This is because a higher $\mathrm{We_{cr}}$ implies that the atomized structures stabilize at higher Weber numbers and, therefore, stop creating interface at higher relative velocities. Among the tested $\mathrm{We_{cr}}$ values, the largest one ($\mathrm{We_{cr}} = 7$) shows still close agreement to DNS, with only about a 20% underestimation at the worst position ($X_{\mathrm{DNS}} = 3\,\mathrm{D_l}$). On the other hand, the choice of $\mathrm{We_{cr}} = 1$ leads to a significant overestimation of Σ. These findings indicate that the IAD model exhibits relatively low sensitivity to the

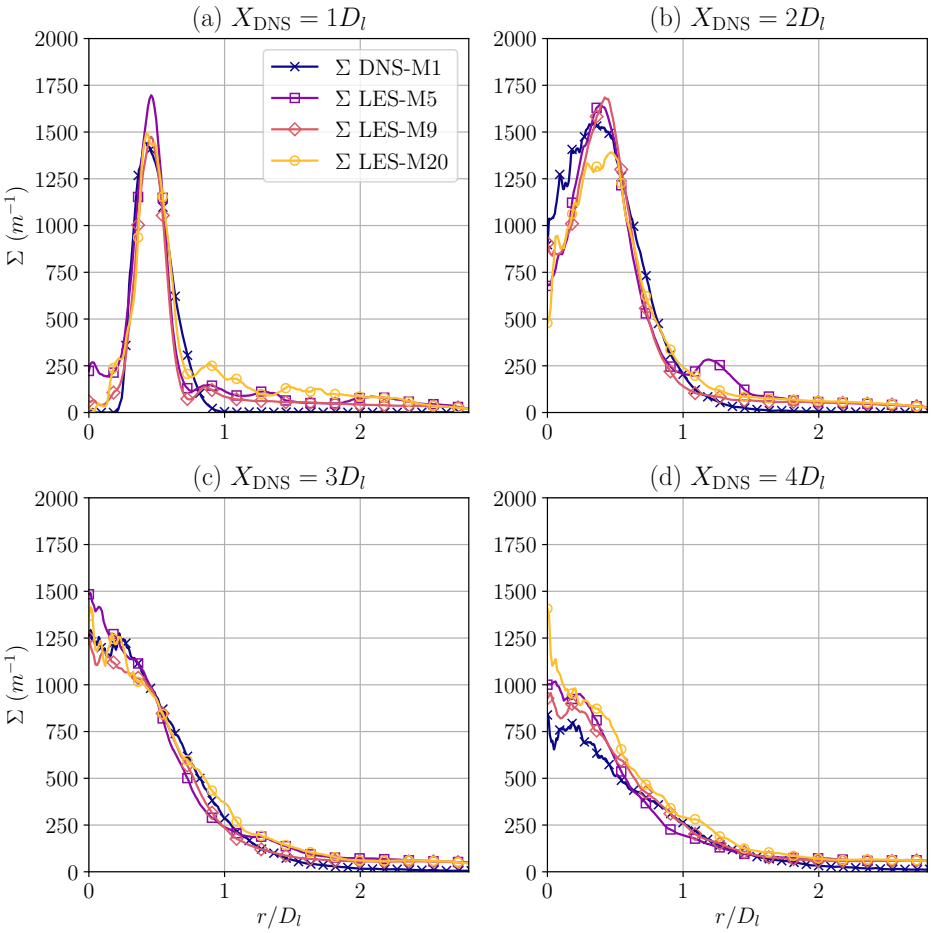

Figure 12: LES-M5, LES-M9, LES-M20, DNS IAD profiles at positions $X_{\mathrm{DNS}} = 1, 2, 3, 4\,\mathrm{D_l}$ for the DNS and at corresponding positions corrected by offsets for LES with $\mathrm{We_{cr}} = 3.5$.

critical Weber number, as long as it is chosen carefully within an appropriate range, preferably overestimated rather than underestimated, such as $\mathrm{We_{cr}}$ values between 3 and 7. Additionally, the critical Weber number values observed by Averseng [51] on periodical planar liquid sheets, falling within the range of 2 to 4, provide further support for the chosen $\mathrm{We_{cr}}$ value in this paper.

7. Conclusion

This paper has presented a comprehensive study on the modeling of coaxial two-phase flows. The proposed approach is based on coupling a diffuse interface dense solver and a subgrid interface area density model to characterize all the relevant scales of the liquid jet assisted atomization. The model has been successfully validated through comparisons with high-fidelity DNS data from Hoarau et al. [16], producing very accurate results for several mesh sizes, thus adapting to the resolution given by the dense phase solver.

Based on Chesnel et al. [34] initial work on IAD applied to Diesel jets, the proposed formulation is adapted to the physics encountered in coaxial jets typically found in LRE. Unlike the mechanical atomization observed in Diesel jets, the atomization in coaxial injectors is primarily driven by the shearing of the liquid by the high-velocity gas, known as assisted atomization. This fundamental difference in the atomization mechanism necessitates the development of a new modeling approach to capture the creation of the interface in this specific application. The model formulation considers several terms related to atomization location, frequency, magnitude, local critical droplet size, and mesh dependence. In the proposed modeling, as the dense phase equilibrium model could not give accurate local liquid and gas velocities, a dedicated modeling of the local liquid/gas relative velocity was proposed and successfully incorporated into the IAD model. It is worth noting that the model could be simplified by directly using both liquid and gas velocities from the Baer-Nunziato 7-equation model, thereby eliminating the need to explicitly model the relative velocity.

A critical Weber number estimates the local equilibrium between surface tension and shearing stress, thus stopping the interface production. In the studied configuration, a $\mathrm{We_{cr}}$ value of 3.5 demonstrates the best agreement with the reference DNS

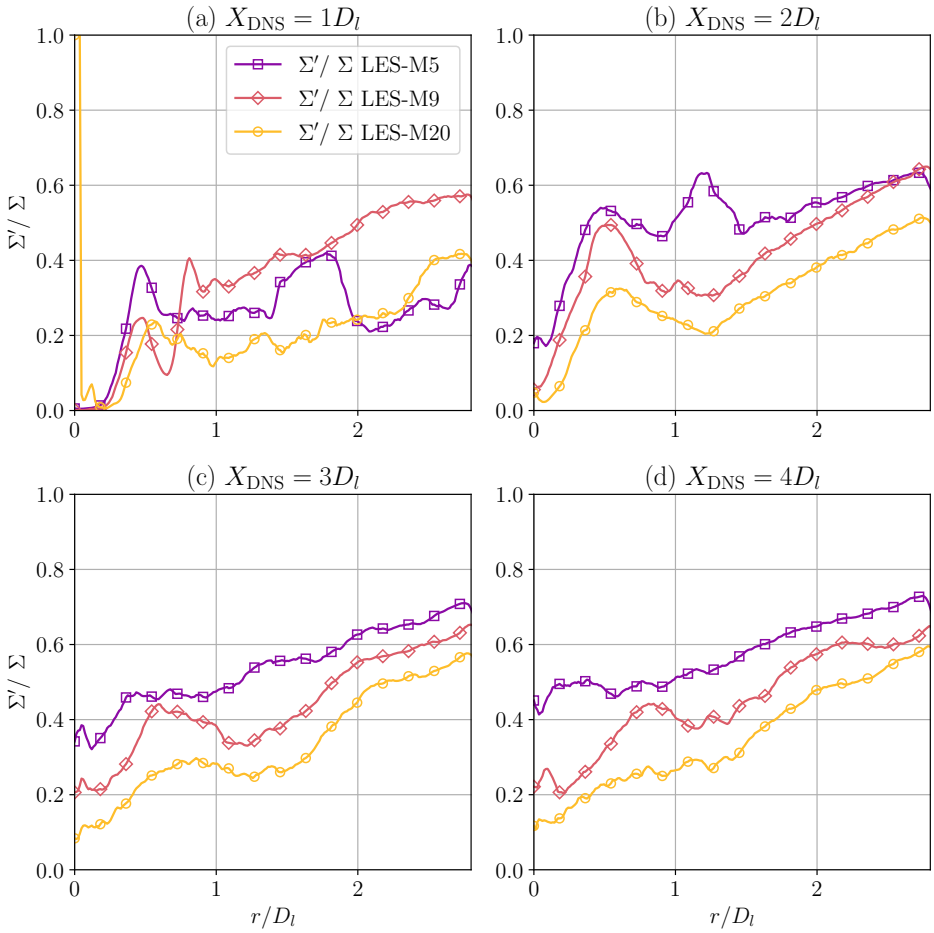

Figure 13: LES-M5, LES-M9, LES-M20 profiles of Σ' over total Σ ratio at positions $X_{\mathrm{DNS}} = 1, 2, 3, 4\,\mathrm{D_l}$ positions corrected by offsets with $\mathrm{We_{cr}} = 3.5$.

data in the primary atomization region. Unsurprisingly, this finding deviates from the prediction of Pilch and Erdman [44], mainly due to the non-spherical nature of atomized structures and the complexity of the turbulent flow produced during primary atomization. Nonetheless, the IAD model exhibits a relatively low sensitivity to the choice of the critical Weber number, as excellent agreements with the reference are achieved within the range of 3 to 7. This favorable characteristic of the model encourages its application in other configurations where reference results are not available, provided that $\mathrm{We_{cr}}$ values close to those determined in this study are selected.

The IAD holds potential for various applications. Firstly, it can be directly employed as an estimation of the interface area of the two-phase full jet, facilitating its evaporation in dense-phase Navier-Stokes solvers. Another application involves using the IAD to define the drop Sauter diameter D_{32} for coupling with LES Eulerian or Lagrangian dispersed phase solvers, as discussed in [37]. This coupling enables the incorporation of droplet dynamics and interactions, crucial in simulating dispersed phase phenomena in multiphase flows [36].

Finally, the proposed modeling approach was specifically applied to the fiber regime of assisted atomization. It is important to note that the formulation of the model can be extended to other regimes of assisted atomization and other configurations, such as jets in cross-flow. The underlying framework of the model can describe the full range of Weber numbers, which encompass various atomization regimes. However, the general applicability of the IAD sub-grid model requires additional validations. In particular, the applicability of the free jet law, which is contingent upon specific initial conditions and assumed configuration-independent coefficients, needs to be thoroughly investigated.

8. Acknowledgments

This work was granted by a PhD grant from CNES (Centre National d'Etudes Spatiales) and ONERA (Office National d'Etudes et de Recherches Aérospatiales). For the purpose of Open Access, a CC-BY public copyright license has been applied by the authors to the present document and will be applied to all subsequent versions up to the author-accepted manuscript arising from this submission.

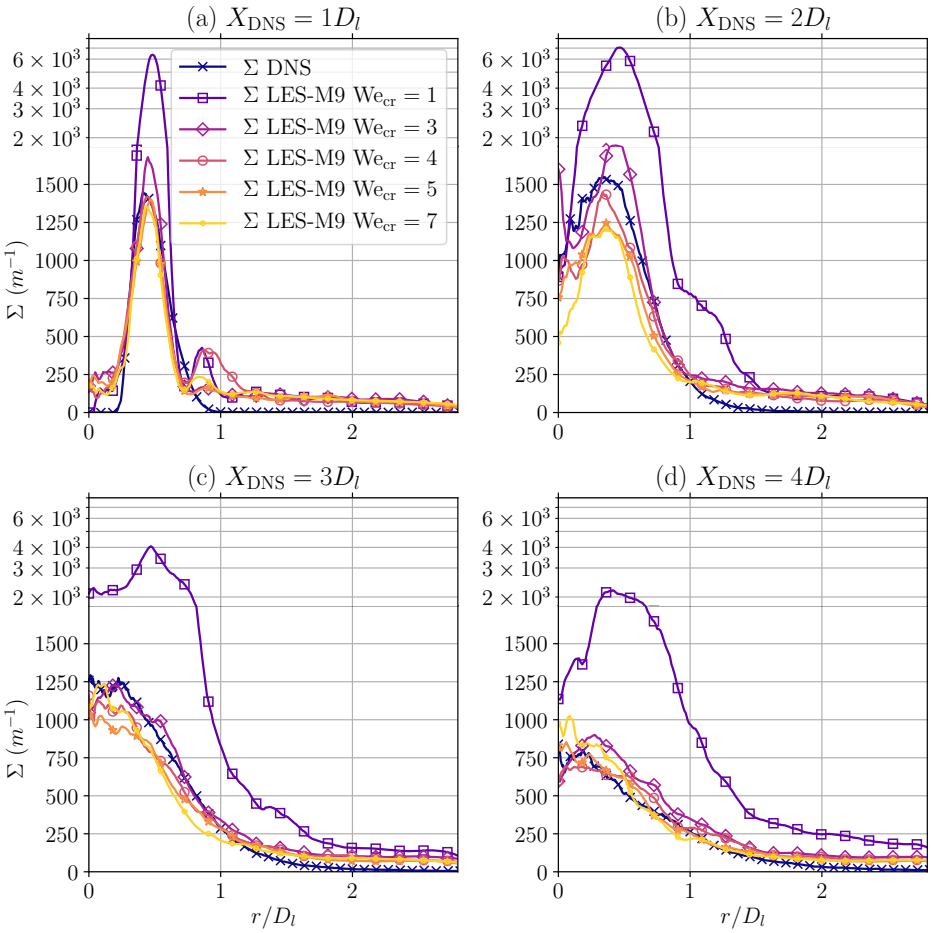

Figure 14: Interface area density profiles at positions $X_{\mathrm{DNS}} = 1, 2, 3, 4\,\mathrm{D_l}$ for the DNS and at corresponding positions corrected by the offset for the LES with $\mathrm{We_{cr}} = 1, 3, 4, 5, 7$ on the LES-M9 mesh.

Appendix A. Sensibility on λ_{atom}

This appendix presents a parametric study that investigates the influence of the coefficients a_λ and b_λ of the λ_{atom} function in the IAD model. Table A.4 provides details of the parameter variations, while Figure A.15 displays the resulting functions. The coefficients a_λ and b_λ control the shape and behavior of the λ_{atom} function, which determines the location of IAD creation. Modifying these coefficients allows us to explore different scenarios and assess their impact on the model predictions.

In Figure A.16, the IAD profiles at positions $X_{\mathrm{DNS}} = 1, 2, 3, 4\,\mathrm{D_l}$ on both DNS and LES-M9 meshes are plotted for the different λ_{atom} functions previously defined. Except for the $\lambda_{\mathrm{atom\ 3}}$ function, the other functions provide consistent results. The $\lambda_{\mathrm{atom\ 3}}$ function underestimates the position of IAD creation due to a relatively low b_λ coefficient, leading to a significant discrepancy between the predicted IAD production and the DNS results. It induces the production of IAD much closer to the backplate than observed on the DNS, in a zone where the velocity gradient between the gas and the liquid is very high. This induces a large overestimation of the IAD production. On the other hand, the $\lambda_{\mathrm{atom\ 4}}$ function has been chosen to study the impact of a slight overestimation of the X_{atom} parameter. This function ex-

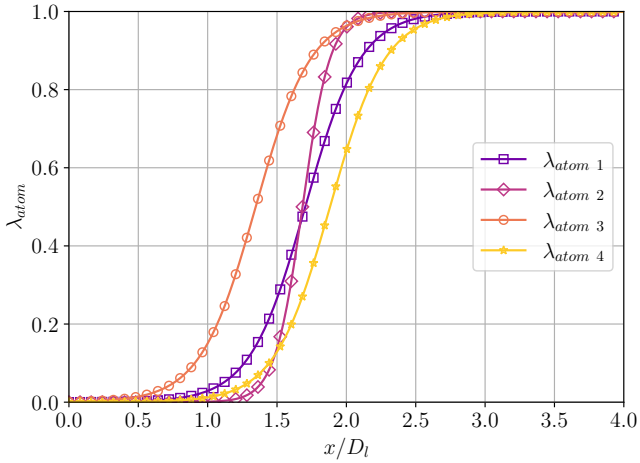

Figure A.15: Atomization location function λ_{atom} for several parameters a_λ, b_λ

	$\lambda_{\text{atom 1}}$	$\lambda_{\text{atom 2}}$	$\lambda_{\text{atom 3}}$	$\lambda_{\text{atom 4}}$
X_{atom}	2.14	2.14	1.79	2.32
$\lambda_{\text{atom}}(X_{\text{atom}})$	0.9	0.99	0.9	0.9
b_λ	5.0	10.0	5.0	5.0
a_λ	1.70	1.68	1.35	1.88

Table A.4: Parameters for the atomization location function λ_{atom}

hibits a maximum underestimation of the IAD production of approximately 10%.

These findings highlight the sensitivity of the IAD model to the choice of the λ_{atom} function and the importance of accurately determining the position of IAD creation for reliable predictions.

References

[1] A. Mansour and N. Chigier. Disintegration of liquid sheets. *Physics of Fluids A*, 2(5):706–719, 1990. ISSN 08998213. doi: 10.1063/1.857724.

[2] C. Larricq-Fourcade. *Etude de la pulvérisation assistée en air d'une nappe liquide et influence d'un vent ionique sur les instabilités hydrodynamiques*. PhD thesis, 2006. URL `http://www.theses.fr/2006ESAE0024`.

[3] V. G. Fernández, G. Lavergne, and P. Berthoumieu. Dynamic primary atomization characteristics in an airblast atomizer, high pressure conditions. *Atomization and Sprays*, 21(1):17–29, 2011. ISSN 10445110. doi: 10.1615/AtomizSpr.v21.i1.20.

[4] B. Déjan. *Etude expérimentale de l'atomisation d'une nappe liquide avec et sans zone de pré-film en vue de sa modélisation - Influence des conditions limites*. PhD thesis, Institut Supérieur de l'Aéronautique et de l'Espace (ISAE), France, 2015. URL `http://www.theses.fr/2015ESAE0032`.

[5] P. Marmottant and E. Villermaux. On spray formation. *Journal of Fluid Mechanics*, 498(498):73–111, 2004. ISSN 00221120. doi: 10.1017/S0022112003006529.

[6] N. Fdida and J. B. Blaisot. Drop size distribution measured by imaging: Determination of the measurement volume by the calibration of the point spread function. *Measurement Science and Technology*, 21(2), 2010. ISSN 13616501. doi: 10.1088/0957-0233/21/2/025501.

[7] N. Fdida, L. Vingert, Y. Mauriot, L. H. Dorey, and M. Théron. Comparison of LOX / Methane and LOX / Hydrogen cryogenic spray combustion with simultaneous optical diagnostics. *Eucass 2019*, pages 2–11, 2019. doi: 10.13009/EUCASS2019-862.

[8] N. Machicoane, R. Osuna-Orozco, and A. Aliseda. Regimes of the length of a laminar liquid jet fragmented by a gas co-flow. *International Journal of Multiphase Flow*, 165:104475, 2023. ISSN 0301-9322. doi: https://doi.org/10.1016/j.ijmultiphaseflow.2023.104475.

[9] N. Odier, G. Balarac, and C. Corre. Numerical analysis of the flapping mechanism for a two-phase coaxial jet. *International Journal of Multiphase Flow*, 106:164–178, 2018. ISSN 0301-9322. doi: https://doi.org/10.1016/j.ijmultiphaseflow.2018.05.028.

[10] T. Mller, A. Snger, P. Habisreuther, T. Jakobs, D. Trimis, T. Kolb, and N. Zarzalis. Simulation of the primary breakup of a high-viscosity liquid jet by a coaxial annular gas flow. *International Journal of Multiphase Flow*, 87:212–228, 2016. ISSN 0301-9322. doi: https://doi.org/10.1016/j.ijmultiphaseflow.2016.09.008.

[11] F. Xiao, M. Dianat, and J. J. McGuirk. LES of turbulent liquid jet primary breakup in turbulent coaxial air flow. *International Journal of Multiphase Flow*, 60:103–118, 2014. ISSN 03019322. doi: 10.1016/j.ijmultiphaseflow.2013.11.013. URL `http://dx.doi.org/10.1016/j.ijmultiphaseflow.2013.11.013`.

[12] H. G. Weller, G. Tabor, H. Jasak, and C. Fureby. A tensorial approach to computational continuum mechanics using object-oriented techniques. *Computer in Physics*, 12(6):620–631, 11 1998. ISSN 0894-1866. doi: 10.1063/1.168744. URL `https://doi.org/10.1063/1.168744`.

[13] F. Zhang, T. Zirwes, T. Mller, S. Wachter, T. Jakobs, P. Habisreuther, N. Zarzalis, D. Trimis, T. Kolb, and D. Stapf. Effect of elevated pressure on air-assisted primary atomization of coaxial liquid jets: Basic research for entrained flow gasification. *Renewable and Sustainable Energy Reviews*, 134:110411, 2020. ISSN 1364-0321. doi: https://doi.org/10.1016/j.rser.2020.110411.

[14] F. Zhang, S. Wachter, T. Zirwes, T. Jakobs, N. Zarzalis, D. Trimis, T. Kolb, and D. Stapf. Effect of nozzle upscaling on coaxial, gas-assisted atomization. *Physics of Fluids*, 35(4):043302, 04 2023. ISSN 1070-6631. doi: 10.1063/5.0141156. URL `https://doi.org/10.1063/5.0141156`.

[15] L. Vu, N. Machicoane, D. Li, T. Morgan, J. Heindel, A. Aliseda, and O. Desjardins. A computational study of a two-fluid atomizing coaxial jet: Validation against experimental back-lit imaging and radiography and the influence of gas velocity and contact line model. *International Journal of Multiphase Flow*, 167:104520, 2023. ISSN 0301-9322. doi: https://doi.org/10.1016/j.ijmultiphaseflow.2023.104520.

[16] J.-C. Hoarau, L.-H. Dorey, D. Zuzio, F. Granger, and J. L. Estivalèzes. Direct numerical simulation of a subcritical coaxial injection in fiber regime using sharp interface reconstruction. *International Journal of Multiphase Flow*, 2024. URL `https://hal.science/hal-04212765`.

[17] S.V. Apte, K. Mahesh, P. Moin, and J.C. Oefelein. Large-eddy simulation of swirling particle-laden flows in a coaxial-jet combustor. *International Journal of Multiphase Flow*, 29(8):1311–1331, 2003. ISSN 0301-9322. doi: https://doi.org/10.1016/S0301-9322(03)00104-6.

[18] J. M. Senoner, M. Sanjosé, T. Lederlin, F. Jaegle, M. García, E. Riber, B. Cuenot, L. Gicquel, H. Pitsch, and T. Poinsot. Eulerian and Lagrangian Large-Eddy Simulations of an evaporating two-phase flow. *C. R. Mecanique*, 337(6-7):458–468, 2009. ISSN 1631-0721. doi: 10.1016/j.crme.2009.06.002.

[19] W. Ranz. Some experiments on orifice sprays. *The Canadian Journal of Chemical Engineering*, 36(4):175–181, 1958. ISSN 1939019X. doi: 10.1002/cjce.5450360405.

[20] N. Chigier and Z. Farago. Morphological Classification of Disintegration of Round Liquid Jets in a Coaxial Air Stream. *Atomization and Sprays*, 2 (2):137–153, 1992. ISSN 1044-5110. doi: 10.1615/atomizspr.v2.i2.50.

[21] K. A. Sallam, C. Aalburg, and G. M. Faeth. Breakup of round nonturbulent liquid jets in gaseous crossflow. *AIAA Journal*, 42(12):2529–2540, 2004. ISSN 00011452. doi: 10.2514/1.3749.

[22] P. K. Wu, K. A. Kirkendall, R. P. Fuller, and A. S. Nejad. Breakup processes of liquid jets in subsonic crossflows. *Journal of Propulsion and Power*, 13(1):1–14, 1996. doi: 10.2514/6.1996-3024.

[23] J. C. Lasheras and E. J. Hopfinger. Liquid jet instability and atomization in a coaxial gas stream. *Annual Review of Fluid Mechanics*, 32(1):275–308, 2000. doi: 10.1146/annurev.fluid.32.1.275. URL `https://doi.org/10.1146/annurev.fluid.32.1.275`.

[24] F. Baillot, J.-B. Blaisot, G. Boisdron, and C. Dumouchel. Behaviour of an air-assisted jet submitted to a transverse high-frequency acoustic field. *Journal of Fluid Mechanics*, 640:305342, 2009. doi: 10.1017/S002211200999139X.

[25] A. Vallet, A. A. Burluka, and R. Borghi. Development of a Eulerian model for the "Atomization" of a liquid jet. *Atomization and Sprays*, 11 (6):619–642, 2001. ISSN 10445110. doi: 10.1615/atomizspr.v11.i6.20.

[26] A. Vallet and R. Borghi. Modélisation eulerienne de l'atomisation d'un jet liquide. *Comptes Rendus de l'Académie de Sciences - Serie IIb: Mécanique, Physique, Chimie, Astronomie*, 327(10):1015–1020, 1999. ISSN 12874620. doi: 10.1016/S1287-4620(00)87013-1.

[27] F.E. Marble and J.E. Broadwell. The Coherent Flame Model for Turbulent Chemical Reactions. Technical report, Purdue University, 1977.

[28] C. Morel. On the surface equations in two-phase flows and reacting single-phase flows. *International Journal of Multiphase Flow*, 33(10): 1045–1073, 2007. ISSN 03019322. doi: 10.1016/j.ijmultiphaseflow.2007.02.008.

[29] S. Jay, F. Lacas, and S. Candel. Combined surface density concepts for dense spray combustion. *Combustion and Flame*, 144(3):558–577, 2006. ISSN 00102180. doi: 10.1016/j.combustflame.2005.07.017.

[30] P. J. O'Rourke and A. A. Amsden. The TAB method for numerical cal-

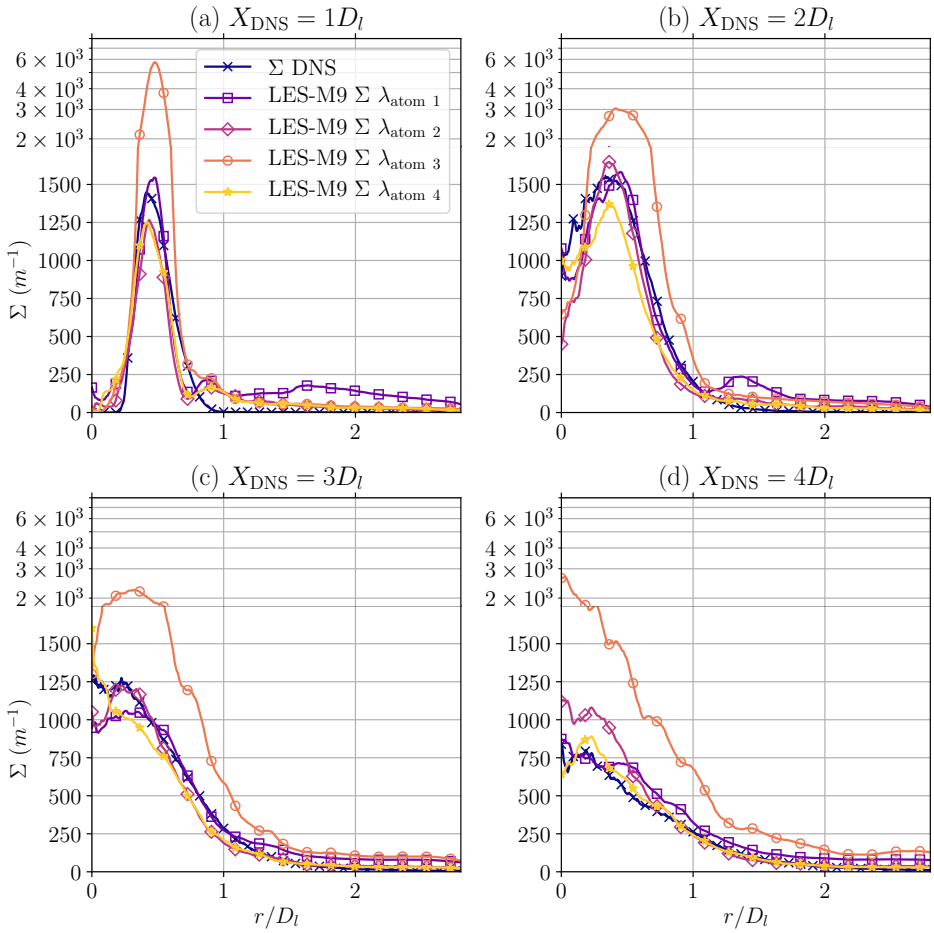

Figure A.16: Interface area density profiles at positions $X_{\mathrm{DNS}} = 1, 2, 3, 4\,\mathrm{D_l}$ for the DNS and at corresponding positions corrected by the offset for LES-M9 mesh for several λ_{atom} functions defined in Table A.4 with $\mathrm{We_{cr}} = 3.5$.

culation of spray droplet breakup. In *International Fuels nad Lubricants Meeting and Exposition*, Toronto, 1987.

[31] R. Lebas, T. Menard, P. A. Beau, A. Berlemont, and F. X. Demoulin. Numerical simulation of primary break-up and atomization: DNS and modelling study. *International Journal of Multiphase Flow*, 35(3):247–260, 2009. ISSN 03019322. doi: 10.1016/j.ijmultiphaseflow.2008.11.005.

[32] P. A. Beau, T. Ménard, R. Lebas, A. Berlemont, S. Tanguy, and F. X. Demoulin. Numerical jet atomization. Part II: modeling information and comparison with DNS results. In *7th International Symposium on numerical methods for multiphase flows*, 2006. ISBN 0791847500. doi: 10.1115/fedsm2006-98166.

[33] B. Duret, J. Reveillon, T. Menard, and F. X. Demoulin. Improving primary atomization modeling through DNS of two-phase flows. *International Journal of Multiphase Flow*, 55:130–137, 2013. ISSN 03019322. doi: 10.1016/j.ijmultiphaseflow.2013.05.004.

[34] J. Chesnel, J. Reveillon, T. Ménard, and F. X. Demoulin. Large eddy simulation of liquid jet atomization. *Atomization and Sprays*, 21(9):711–736, 2011. ISSN 10445110. doi: 10.1615/AtomizSpr.2012003740.

[35] A. Ficuciello, J. B. Blaisot, C. Richard, and F. Baillot. Investigation of air-assisted sprays submitted to high frequency transverse acoustic fields: Droplet clustering. *Physics of Fluids*, 29(6):1–17, 2017. ISSN 10897666. doi: 10.1063/1.4985202.

[36] N. Rutard, L. H. Dorey, C. Le Touze, and S. Ducruix. Large-eddy simulation of an air-assisted liquid jet under a high-frequency transverse acoustic forcing. *International Journal of Multiphase Flow*, 122:103144, 2020. ISSN 03019322. doi: 10.1016/j.ijmultiphaseflow.2019.103144.

[37] C. Le Touze, L. H. Dorey, N. Rutard, and A. Murrone. A compressible two-phase flow framework for Large Eddy Simulations of liquid-propellant rocket engines. *Applied Mathematical Modelling*, 84:265–286, 2020. ISSN 0307904X. doi: 10.1016/j.apm.2020.03.028.

[38] M. R. Baer and J. W. Nunziato. A two-phase mixture theory for the deflagration-to-detonation transition (ddt) in reactive granular materials. *International Journal of Multiphase Flow*, 12(6):861–889, 1986. ISSN 03019322. doi: 10.1016/0301-9322(86)90033-9.

[39] F. Nicoud, H. B. Toda, O. Cabrit, S. Bose, and J. Lee. Using singular values to build a subgrid-scale model for large eddy simulations. *Physics of Fluids*, 23(8), 2011. ISSN 10706631. doi: 10.1063/1.3623274.

[40] J. U. Brackbill, D. B. Kothe, and C. Zemach. A continuum method for modeling surface tension. *Journal of Computational Physics*, 100(2):335–354, 1992. ISSN 10902716. doi: 10.1016/0021-9991(92)90240-Y.

[41] D. Gueyffier, J. Li, A. Nadim, R. Scardovelli, and S. Zaleski. Volume-of-Fluid Interface Tracking with Smoothed Surface Stress Methods for Three-Dimensional Flows. *Journal of Computational Physics*, 152:423–456, 1999. doi: 10.1006/jcph.1998.6168.

[42] A. Chiapolino, P. Boivin, and R. Saurel. A simple and fast phase transition relaxation solver for compressible multicomponent two-phase flows. *Computers and Fluids*, 150:31–45, 2017. ISSN 00457930. doi: 10.1016/j.compfluid.2017.03.022.

[43] C. Le Touze and N. Rutard. Numerical methods for diffuse interface multifluid models. In *ECCOMAS*, pages 1–12, 2022.

[44] M. Pilch and C. A. Erdman. Use of breakup time data and velocity history data to predict the maximum size of stable fragments for acceleration-induced breakup of a liquid drop. *International Journal*

of Multiphase Flow, 13(6):741–757, 1987. ISSN 03019322. doi: 10.1016/0301-9322(87)90063-2.

[45] J. O. Hinze. Fundamentals of the hydrodynamic mechanism of splitting in dispersion processes. *AIChE Journal*, 1(3):289–295, 1955. ISSN 15475905. doi: 10.1002/aic.690010303.

[46] L. Schiller and Z. Naumann. A drag Coefficient Correlation. *VDI Zeitung*, 77:318–320, 1935.

[47] G. Blanchard. *Modélisation et simulation multi-échelles de l'atomisation d'une nappe liquide cisaillée*. PhD thesis, Institut Supérieur de l'Aéronautique et de l'Espace (ISAE), France, 2014. URL `https://hal.science/tel-01171809`.

[48] T. G. Malmström, A. T. Kirkpatrick, B. Christensen, and K. D. Knappmiller. Centreline velocity decay measurements in low-velocity axisymmetric jets. *Journal of Fluid Mechanics*, 346:363–377, 1997. ISSN 00221120. doi: 10.1017/S0022112097006368.

[49] H. B. Awbi. *Ventilation of Buildings*. Routledge, 2003. ISBN 9780415270564.

[50] G. Cao, C. Kandzia, D. Müller, J. Heikkinen, R. Kosonen, and Mika Ruponen. Experimental study of the effect of turbulence intensities on the maximum velocity decay of an attached plane jet. *Energy and Buildings*, 65:127–136, 2013. ISSN 03787788. doi: 10.1016/j.enbuild.2013.05.041.

[51] M. Averseng. *Contribution à la modélisation de l'atomisation assistée par l'analyse de simulations haute fidélité*. PhD thesis, Institut Supérieur de l'Aéronautique et de l'Espace (ISAE), France, 2022. URL `https://hal.science/tel-04119166`.